

Letter of Intent for Jefferson Lab PAC 43

**Timelike Compton Scattering
on the transversely polarized proton at 11 GeV**

T. Horn, A. Mkrtchyan*, M. Carmignotto, I. Sapkota
Catholic University of America, Washington, D.C. 20064

A. Asaturyan, H. Mkrtchyan, V. Tadevosyan†, S. Zhamkochyan
A. I. Alikhanyan National Science Laboratory, 0036 Yerevan, Armenia

A. Camsonne, R. Ent, P. Nadel-Turoński‡, B. Wojtsekhowski, S.A. Wood
Thomas Jefferson National Accelerator Facility, Newport News, Virginia 23606

M. Boer§, M. Guidal, C. Munoz Camacho, R. Paremuzyan
Institut de Physique Nucleaire d'Orsay, IN2P3, BP 1, 91406 Orsay, France

I. Albayrak
Akdeniz University, Antalya, Turkey

D. Day
University of Virginia, Charlottesville, VA 22904

C. Hyde, M.N.H. Rashad
Old Dominion University, Norfolk, Virginia 23529

J. Roche
Ohio University, Athens, OH 45701

And the NPS Collaboration.

(Dated: May 18, 2015)

*Co-spokesperson and Contact person

†Co-spokesperson

‡Co-spokesperson

§Co-spokesperson

Abstract

We propose to study Timelike Compton Scattering (TCS) on a transversely polarized proton with quasi-real photons using the reaction $ep \rightarrow \gamma^* p' \rightarrow e^+ e^- p'(e')$.

Deeply Virtual Compton Scattering (DVCS) is the simplest and cleanest way to access the Generalized Parton Distributions (GPDs) of the nucleon. The DVCS process interferes with the Bethe-Heitler process allowing one to access the DVCS amplitudes. Time-like Compton Scattering (TCS) is the inverse process of (spacelike) DVCS, where the hard scale is provided by the virtuality of the final-state photon (or the invariant mass of the produced lepton pair).

The measurement of TCS spin asymmetries with a transversely polarized target is particularly sensitive to the imaginary part of \tilde{H} and E , and in the case of double-spin asymmetries, also the real part of the amplitude. Having several independent observables is important for reducing the uncertainty of the fits aimed at extracting Compton Form Factors, making this proposed experiment complementary to the approved CLAS12 experiment E12-12-001 [9], which will use polarized photon beam but an unpolarized hydrogen target. The fitting uncertainties are further significantly reduced by combining TCS and DVCS data. Measuring the full set of observables for both processes is thus critical for the JLab 12 GeV GPD program. A comparison of TCS and DVCS results is also the most straightforward way of testing the universality (process-independence) of GPDs, and thus of significance to all GPD studies.

In this proposed experiment we will use 11 GeV polarized electrons impinging on a transversely polarized solid ammonia NH_3 target. This proposed experiment can run in Hall C or Hall A, and will use pair of NPS spectrometers to detect leptons and wide acceptance hodoscope systems for recoil protons. The projections are shown for 30 days of running.

Contents

1. Introduction	4
2. Physics of Timelike Compton Scattering	6
A. Physics motivations	6
1. Timelike Compton Scattering and Generalized Parton Distributions	6
2. Photoproduction of a lepton pair	8
B. Theoretical predictions	10
1. Cross section	10
2. Single spin asymmetry: circularly polarized beam	12
3. Single spin asymmetry: transversely polarized target	13
4. Double spin asymmetries: circularly polarized beam and transversely polarized target	16
5. Conclusions	16
C. TCS at JLab 6 GeV	17
3. Experimental Setup	21
A. Lepton detectors	21
B. Detection of recoil protons	23
C. Tracker	24
D. Polarized Target	25
4. Experiment Kinematics and Projected Results	29
A. Kinematics of proposed experiment	30
B. Acceptance	31
C. TCS Analysis	32
D. Projections	33
1. Counting rates	34
5. Systematic Uncertainties	35
6. Beam Time	36
References	37

1. INTRODUCTION

Hard exclusive processes on the proton provide access to the Generalized Parton Distributions (GPDs) [1–4] which contain information about the longitudinal momentum and the spatial transverse distributions of partons inside the proton (in a frame where the nucleon has an infinite momentum along its longitudinal direction).

Both Deeply Virtual Compton Scattering (DVCS) and Timelike Compton Scattering (TCS) are two limiting cases of the hard exclusive General Compton Scattering (GCS) process: $\gamma^*(q) + P(p) \rightarrow \gamma^*(q') + P(p')$. GCS is the scattering of a high-energy virtual photon off a quark inside the proton (the four-momenta q and q' of the photons can have any virtuality).

In DVCS and TCS processes one of the photons (initial or final) is on shell (real) while other is virtual. Spacelike Deeply Virtual Compton Scattering (DVCS) corresponds to the case where the incoming photon is emitted by a lepton beam and has a high spacelike virtuality and where the final photon is real ($eP \rightarrow \gamma P$ or $\gamma^* \rightarrow \gamma P$). The DVCS process interferes with the Bethe-Heitler process allowing one to access the DVCS amplitudes.

The DVCS or TCS amplitude can be factorized into an elementary “hard” (perturbative) scattering process $\gamma^*q \rightarrow \gamma q$ (where q is a quark of the proton), which can be calculated perturbatively, and a “soft” (non-perturbative) QCD bilocal matrix elements. The Fourier transforms into momentum space of these QCD matrix elements are the so-called Generalized Parton Distributions (GPDs). In DVCS or TCS on the nucleon, there are at QCD leading-twist order four quark helicity conserving GPDs (H , E , \tilde{H} , and \tilde{E}). These can be accessed and which correspond to the four independent helicity-spin transitions between the initial quark-proton system and the final one.

DVCS is currently widely investigated, experimentally as well as theoretically. Ref. [4] compiles all existing data in the valence region and presents a first look of the partonic structure of the proton that can be extracted, within some approximations, from the early DVCS data through the GPD formalism. One example of a pioneering result is the first quantitative evaluation of the increase of the transverse size of the proton as smaller longitudinal momentum fractions of partons are probed.

Timelike Compton Scattering (TCS), $\gamma P \rightarrow \gamma^* P$ or $\gamma P \rightarrow e^+e^- P$, is the inverse process of DVCS. It corresponds to the case where the incoming photon is real and the final photon has a high timelike virtuality and decays into a lepton pair. As for DVCS, it can be considered as a very clean process for the studies of the GPDs, as the only soft part of the process is the one associated with the nucleon structure. Therefore TCS provides a new, promising way to access to the GPDs of the nucleon that is complementary to spacelike DVCS. In fact, at leading order in α_s and at leading twist, the DVCS and TCS amplitudes are complex conjugate [2]. As a consequence, the study of both DVCS and TCS in parallel will allow for testing the universality

of the GPDs - an important theoretical question - without any additional unknowns.

Experimentally, the GPDs are not accessed directly, but through the measurement of the Compton Form Factors (CFFs) that can be extracted with several fitting methods [5]. As each observable typically is a combination of contributions from different CFFs, the precision in simultaneously fitting the real and imaginary parts of all four CFFs is mostly driven by the availability of precision data for independent observables. As DVCS and TCS CFFs are the same (at leading order and leading twist), fitting both DVCS and TCS observables together will thus provide a better constrained system to extract the CFFs and access to the GPDs than could be achieved with either process alone.

TCS was originally investigated in terms of GPDs about ten years ago in Ref. [6]. In this pioneering work, analytical formulas in terms of GPDs were derived for the unpolarized and the circularly polarized beam cross sections of the process $\gamma P \rightarrow P' e^+ e^-$ on an unpolarized proton target. Cross section of TCS with the linearly polarized beam are presented in article [7]. In a more recent theoretical work [8], all unpolarized and beam (circularly or linearly) and/or target (longitudinally or transversally) polarized cross sections were derived, and studies of kinematical and angular dependencies of the cross sections at typical JLab energies were presented. All the possible combinations of single- and double spin asymmetries were presented with different scenarios of the GPDs parameterizations, providing visual pictures of the sensitivities of the different observables to the GPDs. In particular, a strong sensitivity was shown for the asymmetries obtained using transversely polarized targets.

The proposed measurement will thus focus on, for the first time, measuring spin asymmetries with a transversely polarized target. The target spin asymmetry with a transversely polarized target spin will provide a straightforward access to the imaginary part of the GPDs \tilde{H} and E , where the measurement of GPD E is particularly important for understanding the spin structure of the nucleon. It may also be We also propose to measure the double spin asymmetry with a transversely polarized target and a circularly polarized beam, which is mostly sensitive to the real part of the TCS amplitude. The measurement of these proposed asymmetries would have a high impact as they are difficult to model and their sensitivity to TCS could make the constraints on the GPD fits comparable to higher-statistics DVCS experiments.

By providing additional observables that are essential for fits, this proposed measurement is complementary to the approved CLAS12 experiment E12-12-001 [9], which will measure the unpolarized TCS cross section and the beam asymmetry (with an unpolarized hydrogen target), as well as to a number of approved DVCS experiments, making it an important part of the JLab 12 GeV GPD program.

The experimental technique of using quasi-real photons (with $Q^2 < 0.1 \text{ GeV}^2$) tagged by detecting the complete final state except for the beam electron, has been demonstrated in the analysis of CLAS 6 GeV data, and is used in the approved CLAS12 experiment E12-12-

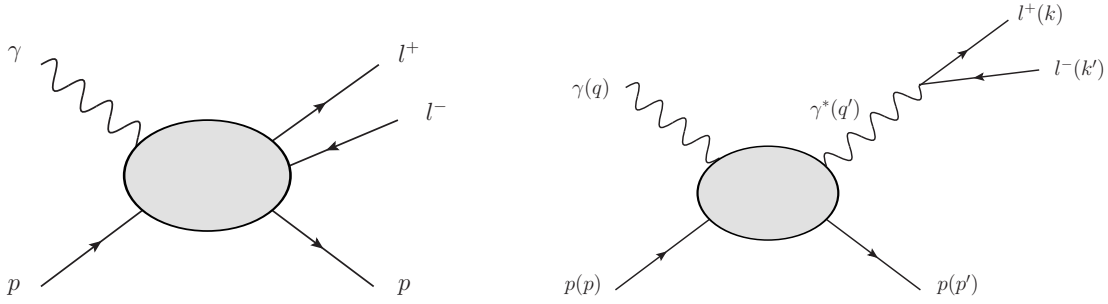


FIG. 1: *Left panel:* Exclusive photoproduction of a lepton pair. *Right panel:* Timelike Compton scattering (TCS). The particle momenta are given in parenthesis.

001 [9]. The experimental setup will further use the UVA transversely polarized solid ammonia NH_3 target, time-of-flight detectors for recoil proton detection, a tracker, and a pair of Neutral Particle Spectrometers (NPS).

2. PHYSICS OF TIMELIKE COMPTON SCATTERING

In this section we describe the theory and phenomenology of the timelike Compton process, discuss observables, and present model calculations. We also explain how the data can be used in global fits, and show 6 GeV analysis results. The physical processes to observe production of a heavy lepton pair, $\gamma + p \rightarrow \mu^+ + \mu^- + p$ or $\gamma + p \rightarrow e^+ + e^- + p$, are exclusive photoproduction and TCS reaction, shown in left panel Fig. 2.

Despite the close analogy to real photon production $ep \rightarrow e\gamma p$ or $\mu p \rightarrow \mu\gamma p$, where DVCS can be accessed, the phenomenology of these reactions shows important differences. In both cases, a Bethe-Heitler (BH) mechanism contributes at the amplitude level. Contrary to the case of DVCS, this contribution always dominates over the one from TCS in the kinematical regime where we want to study it.

A. Physics motivations

1. Timelike Compton Scattering and Generalized Parton Distributions

Timelike Compton Scattering (TCS) off the proton corresponds to the scattering of a photon off a quark, where incoming photon is real and the outgoing one has a large virtuality ($Q'^2 = +q'^2 = (k + k')^2 \gg m_N^2$, where m_N is proton mass). The virtual photon decays into a

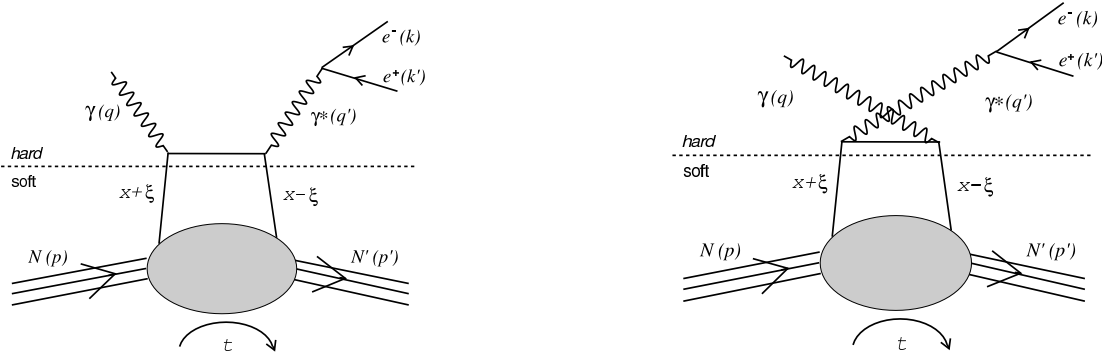


FIG. 2: Leading order, leading twist TCS *handbag* diagram. The dotted line shows the hard-soft factorization.

lepton pair. TCS is studied through the reaction

$$\gamma(q) P(p) \rightarrow \gamma^*(q') P'(p') \rightarrow e^-(k) e^+(k') P'(p') \quad (1)$$

Fig. 2 shows the two diagrams which are involved at leading order and at leading twist. The high virtuality (Q'^2) of the outgoing photon provides hard scale that makes the reaction sensitive to the partonic structure of the nucleon and allows factorization into a calculable hard part ($\gamma q \rightarrow \gamma^* q'$), and a soft part which can be parametrized by the GPDs. The four leading twist GPDs ($H, \tilde{H}, E, \tilde{E}$) depend on the variables (x, ξ, t) , where x is the average (non-measurable) momentum of the struck quark, ξ is the longitudinal momentum transfer, and $t = (p' - p)^2 = (q - q')^2$ is the momentum transfer to the proton (following the notation of Fig. 2). The regime where we have a GPD interpretation of TCS correspond to $Q'^2 \gg m_N^2$ and to a small momentum transfer t , such that $t/Q'^2 \ll 1$, to ensure that the factorization illustrated in Fig. 2 will apply with minimum corrections. From DVCS and Deep Inelastic Scattering (DIS) analysis and experience, it is believed that $Q'^2 > 2 \text{ GeV}^2$ and $-t < 1 \text{ GeV}^2$ (or $\frac{-t}{Q'^2} < 30\%$) - although in the case of TCS, the timelike nature of the outgoing photon also requires Q'^2 to be outside the mass range of the meson resonances in the di-lepton system.

In the asymptotic limits (neglecting terms in t/Q'^2), the variable ξ is defined as

$$\xi = \frac{Q'^2}{2s - Q'^2}. \quad (2)$$

with s the center of mass energy, which is defined by

$$s = (p + q)^2 = m_N^2 + 2 E_\gamma m_N, \quad (3)$$

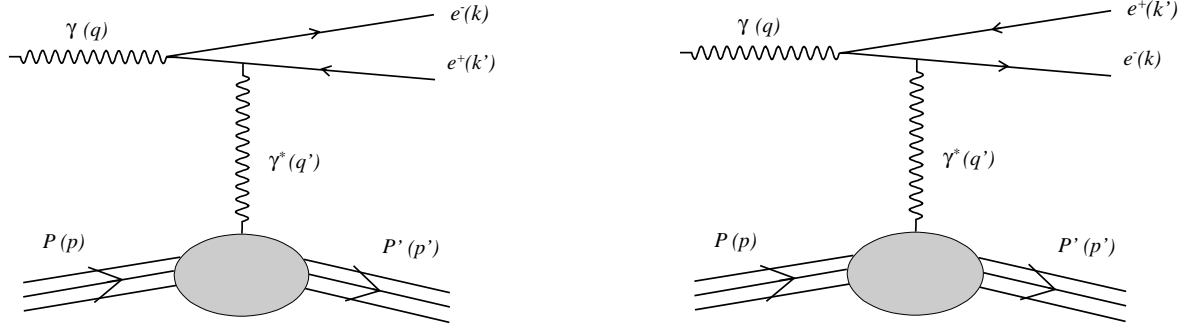


FIG. 3: Diagrams for the Bethe-Heitler process, which produces the same final state as TCS.

in the frame of target proton at rest and where E_γ is the incoming photon energy. Experimentally, one should consider the squared center-of-mass energy of the incoming photon and target proton $s = (q + p)^2 > \approx 2 \text{ GeV}^2$, in order to minimize possible contributions from the Dalitz decay of nucleon resonances.

In the asymptotic limit, following Ji notations [10], the hadronic matrix element can be decomposed into GPDs as follows

$$\begin{aligned}
 H_{\mu\nu} & \quad (4) \\
 &= \frac{1}{2} (-g_{\mu\nu})_\perp \int_{-1}^1 dx \left(\frac{1}{x - \xi - i\epsilon} + \frac{1}{x + \xi + i\epsilon} \right) \cdot \left(H(x, \xi, t) \bar{u}(p') / n u(p) + E(x, \xi, t) \bar{u}(p') i\sigma^{\alpha\beta} n_\alpha \frac{\Delta_\beta}{2m_N} u(p) \right) \\
 & - \frac{i}{2} (\epsilon_{\nu\mu})_\perp \int_{-1}^1 dx \left(\frac{1}{x - \xi - i\epsilon} - \frac{1}{x + \xi + i\epsilon} \right) \cdot \left(\tilde{H}(x, \xi, t) \bar{u}(p') / n \gamma_5 u(p) + \tilde{E}(x, \xi, t) \bar{u}(p') \gamma_5 \frac{\Delta \cdot n}{2m_N} u(p) \right).
 \end{aligned}$$

This decomposition is similar to the one proposed for DVCS in Ref. [11].

2. Photoproduction of a lepton pair

TCS interferes with Bethe-Heitler process, which has the same final state (Fig. 3). In JLab 12 GeV kinematics, where the BH cross section is significantly larger than the TCS cross section, one can take advantage of this interference to enhance the TCS signal.

At fixed beam energy E_γ (or fixed ξ), the $\gamma(q)N(p) \rightarrow N'(p')e^-(k)e^+(k')$ depend on four independent kinematic variables, which can be choose to be Q'^2 , t and the decay angles

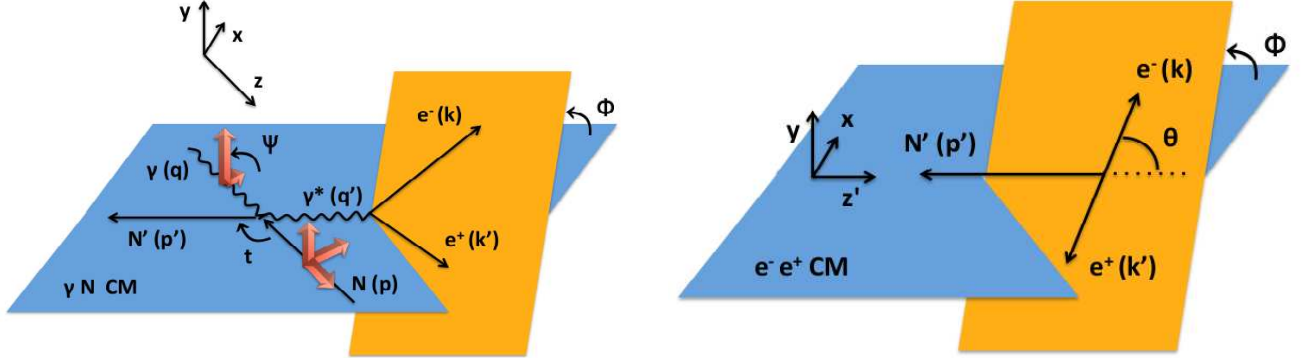


FIG. 4: Left panel: The $\gamma N \rightarrow \gamma^* N'$ reaction (TCS) in the γN CM frame. The red arrows show the photon and target polarization vectors. Right panel: Angles in the lepton CM frame.

of the lepton pair ϕ and θ , which are defined in the rest frame of the virtual photon. There are indicated in Fig. 4. The three red arrows represented on the incoming proton on the left panel shows the 3 possible target polarization directions. Longitudinal polarization is defined according to the proton direction, while the transverse polarizations axes are defined as x when the polarization vector is in reaction plane and as y when the polarization vector is perpendicular to the reaction plane - although in an actual measurement angle between the reaction plane and target polarization vector would vary event-by-event. The two red arrows correspond to the two polarization states for a linearly polarized photon beam, with a polarization vector at an angle Ψ with respect to the reaction plane. The ϕ and θ angles are defined as azimuthal and polar angle of the electron with respect to the boost axis between $\gamma^* P'$ CM frame and γ^* CM frame (virtual photon's direction in $\gamma^* P'$ CM frame). A simple expression for the TCS+BH cross section is

$$\frac{d^4\sigma(\gamma p \rightarrow p' e^+ e^-)}{dQ^2 dt d\Omega} = \frac{|T^{BH} + T^{TCS}|^2}{64 (2\pi)^4 (s - m_N^2)^2} \quad (5)$$

where $d\Omega = d\cos\theta d\phi$.

For the unpolarized cross section, the sum of BH and TCS amplitudes $|T^{BH} + T^{TCS}|^2$ is averaged over the proton and photon helicities, while for polarized cross sections, the helicities of beam and/or target are fixed.

In following subsection, the beam and/or target spin asymmetries will be presented as a function of ϕ or as a function of t . The notation we will use is

- $A_{\odot U}$ circularly beam polarized asymmetry

- A_{U_i} transversely target polarized asymmetry (where i stands for x or y)
- $A_{\odot i}$ double spin asymmetry with a circularly beam polarized and a transversely polarized target

Single spin asymmetries are defined by:

$$A_{\odot U} (A_{U_i}) = \frac{\sigma^+ - \sigma^-}{\sigma^+ + \sigma^-} \quad (6)$$

where σ^\pm stands for the 4-differential cross section $\frac{d^4\sigma}{dQ'^2 dt d\Omega}$, i stands for polarization index of the target and \odot stands for the polarization index of the beam. The + and - exponents respectively represent the direction of the polarization vectors. Double spin asymmetries are defined as

$$A_{\odot i} = \frac{(\sigma^{++} + \sigma^{--}) - (\sigma^{+-} + \sigma^{-+})}{\sigma^{++} + \sigma^{--} + \sigma^{+-} + \sigma^{-+}} \quad (7)$$

where $\sigma_{\pm\pm}$ stands for the 4-differential cross section $\frac{d^4\sigma}{dQ'^2 dt d\Omega}$, i stands for polarization index of the target and \odot stands for the polarization index of the beam.

B. Theoretical predictions

The following theoretical predictions are from [8] using the VGG model for the GPDs [11–13]. While the main focus of this proposed experiment is on the single- and double target spin asymmetries using a transversely polarized target, the cross section and beam spin asymmetries can be used for cross check with other experiments (such as E12-12-001).

1. Cross section

Fig. 5 shows the calculation by Ref. [8] of the ϕ -dependence of the 4-fold differential cross section $\frac{d\sigma_{BH}}{dQ'^2 dt d\phi d(\cos\theta)}$ for the $\gamma P \rightarrow P' e^+ e^-$ reaction (i.e. BH+TCS), at $\eta = 0.2$, $-t = 0.4$ GeV², $Q'^2 = 7$ GeV² and for 3 θ values. The ϕ -distribution depends on θ . As θ tends to 0° , the ϕ distribution peaks towards $\phi=180^\circ$ and as θ tends to 180° , the ϕ -distribution peaks towards $\phi=0^\circ$ (or 360°). There is a smooth transition between these two behaviors for intermediate θ values. For instance, at $\theta=90^\circ$, there are only two small "bumps" at $\phi=0^\circ$ and $\phi=180^\circ$.

These particular shapes are due to the BH process and its singularities. Indeed, in the BH process, when the electron (positron) is emitted in the direction of the initial photon, i.e. $\theta=0^\circ$ ($\theta=180^\circ$), the propagator of the positron (electron) becomes singular and creates a peak in the ϕ distribution at $\phi=180^\circ$ ($\phi=0^\circ$). Intuitively, $\theta=0^\circ$ ($\theta=180^\circ$) forces all particles to be in the same plane, i.e. $\phi=180^\circ$ ($\phi=0^\circ$). The kinematics $\theta=0^\circ$, i.e. the electron is in the direction of

the photon beam, corresponds to $\phi=180^\circ$ because the virtual photon is emitted by the positron, not the electron (see Fig. 5).

We display also in Fig. 5 (left panel) the contribution of TCS alone. In this calculation, we have used only the GPD H . The inclusion of the other GPDs barely changes the result. In contrast to the BH, the TCS is almost flat in ϕ for all θ values. It is clear that the process $\gamma P \rightarrow P'e^+e^-$ is largely dominated by the BH. There is never less than one order of magnitude between BH and TCS.

In Fig. 5 (right panel), we show the curves BH+TCS as well as the BH alone for $\theta=45^\circ$ and $\theta=90^\circ$. Only at $\theta=90^\circ$, where one is far from the two BH singularities, we have a visible difference between the two curves and therefore a sensitivity to TCS. It is of the order of 30% at $\phi=180^\circ$. As one gets closer to one of the two BH singularities ($\theta=45^\circ$ for instance), the two curves BH and BH+TCS are essentially indistinguishable and there is no sensitivity to TCS.

Finally, we show in Fig. 5 the results of the calculations of Ref. [8] for BH+TCS and BH alone for θ integrated over the range $[\pi/4, 3\pi/4]$. In order to maximize count rates, it is interesting to integrate over θ . One still has a sensitivity to TCS. However, it is of the order of 5%, i.e. less than at fixed $\theta=90^\circ$: the integration over θ dilutes the sensitivity to TCS.

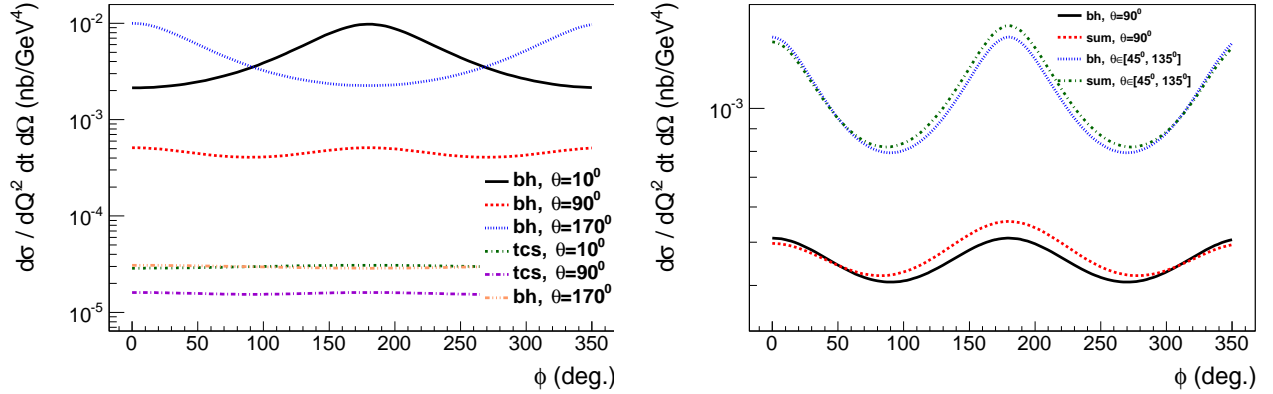


FIG. 5: Left panel: Unpolarized cross section $\frac{d\sigma}{dQ^2 dt d\phi d(\cos\theta)}$ for the process $\gamma P \rightarrow P'e^+e^-$ (for BH + TCS and TCS alone) as a function of ϕ , at $\eta=0.2$, $-t = 0.4$ GeV², $Q'^2 = 7$ GeV² for different fixed θ values: 10° , 90° , 170° for the BH and for the TCS cross sections. Right panel: Comparison between unpolarized cross section for BH alone and for BH+TCS for $\theta = 45^\circ$, 90° and for θ integrated over $[\pi/4, 3\pi/4]$.

To emphasize the D-term sensitivity in unpolarized cross section [14], we also display in Fig. 6 the three-fold differential cross section $\frac{d\sigma_{BH}}{dQ'^2 dt d\phi}$ for $\eta = 0.2$, $-t = 0.4$ GeV² and θ

integrated over the range $[\pi/4, 3\pi/4]$. It modifies the amplitude of the cross section, mostly at $\phi = 0$ and at $\phi = \pi$, by about 10%.

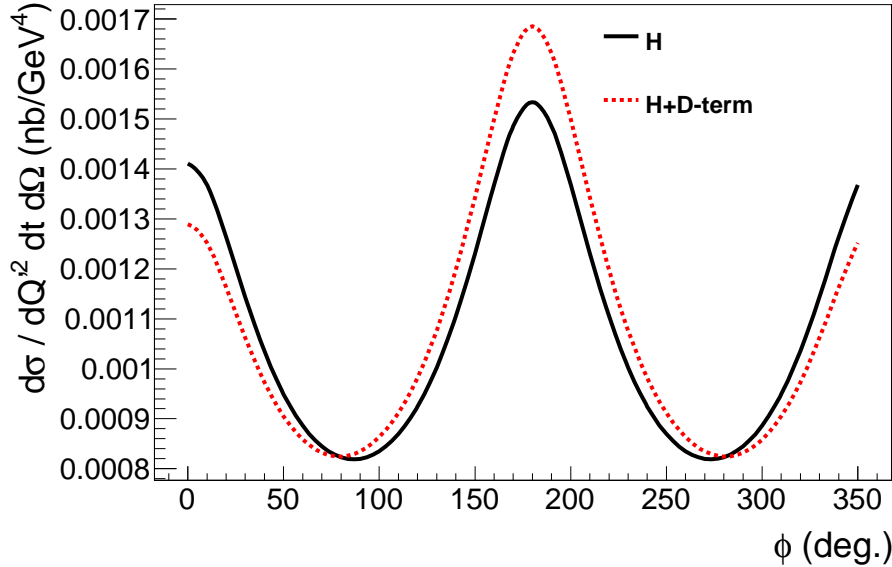


FIG. 6: Unpolarized cross section $\frac{d\sigma}{dQ^2 dt d\phi d(\cos\theta)}$ for the process $\gamma P \rightarrow P' e^+ e^-$ (for BH + TCS and TCS alone) as a function of ϕ , at $\eta=0.2$, $-t = 0.4 \text{ GeV}^2$, $Q'^2 = 7 \text{ GeV}^2$ and for θ integrated over $[\pi/4, 3\pi/4]$, with of without the D-term included in calculations.

Fig. 7 shows the cross sections for BH and for TCS as a function of t and Q'^2 . It has been shown in [6] that TCS cross section is always suppressed with respect to BH cross section, and that TCS signal could be accessed through interference with BH. At JLab typical kinematics, the ratio of TCS/BH will always be around 1 or 2 order of magnitude.

For experimental measurements in Hall C, we plan to focus mostly on beam and/or target spin asymmetries which are more sensitive to the GPDs. Nevertheless, the measurement of the unpolarized cross section was already approved to run [9] and it would be a crucial point to also measure it in Hall C to get independent check of the results and for the studies of systematic effects. In addition, it has been shown that this observable is very sensitive to the real part of the Compton Form Factors and that an experimental measurement will provide very huge constrains for GPD models [11–13].

2. Single spin asymmetry: circularly polarized beam

The beam asymmetry with a circularly polarized beam is defined as:

$$A_{\odot U} = \frac{\sigma^+ - \sigma^-}{\sigma^+ + \sigma^-}, \quad (8)$$

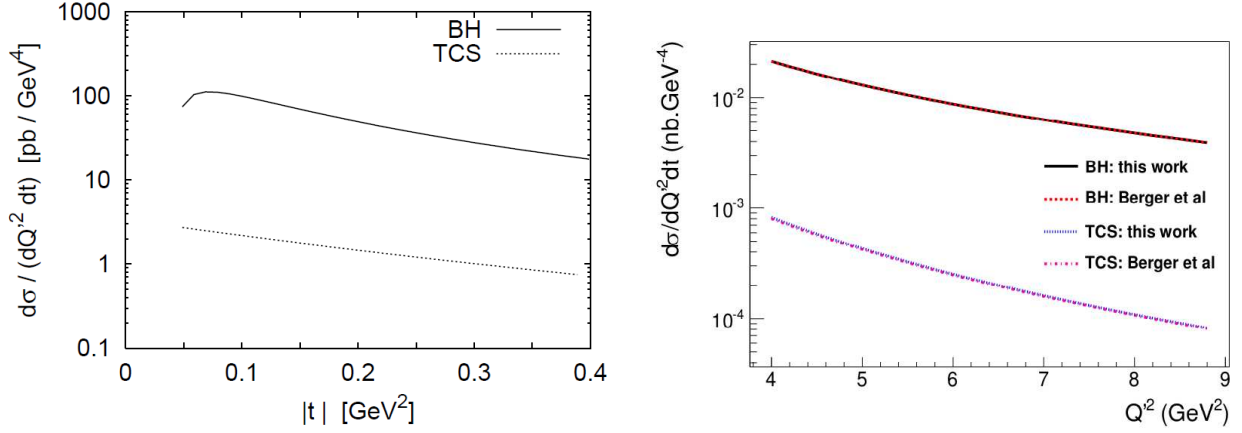


FIG. 7: The two-fold differential cross section $d\sigma/dQ^2 dt$ for BH (highest curves) and TCS (lowest curves) as a function of $|t|$ for $s^{1/2} = 5 \text{ GeV}$ and $Q^2 = 5 \text{ GeV}^2$ (left panel, Ref. [6]) and as a function of Q^2 for $\xi = 0.2$ and $t = 0.4 \text{ GeV}^2$ (right panel). The calculations have been integrated over $\phi \in [0, 2\pi]$ and $\theta \in [\pi/4, 3\pi/4]$. On the right panel the solid curves are our calculations from [8] while the dashed curves are from Ref. [6].

where σ^\pm stands for the 4-fold differential cross sections $\frac{d\sigma}{dQ^2 dt d\phi d(\cos\theta)}$ for the two photon spin states, right and left polarized. We display in Fig. 8 (top panel) the results for $A_{\odot U}$ as a function of ϕ at $Q^2 = 7 \text{ GeV}^2$, $\eta = 0.2$, $-t = 0.4 \text{ GeV}^2$ for θ integrated over $[45^\circ, 135^\circ]$, as calculated by Ref. [8]. We observe that the BH doesn't produce any asymmetry. Any non-zero result therefore reflects the contribution from TCS. This is due to the fact that this observable is sensitive to the imaginary part of the amplitude and that the BH amplitude is purely real. The different curves correspond to different GPDs parametrizations for TCS. In Fig. 9, we show for $\eta = 0.2$, $Q^2 = 7 \text{ GeV}^2$, $\phi = 90^\circ$ and θ integrated over $[45^\circ, 135^\circ]$, the t -dependence of $A_{\odot U}$ and its sensitivity to different GPDs. We notice that the magnitude of $A_{\odot U}$ increases with $|t|$ and that there is a sensitivity of this observable to all four GPDs. We also display in this figure the results with the factorized ansatz for the t -dependence of the H GPD in order to illustrate the model-dependence of the calculation.

3. Single spin asymmetry: transversely polarized target

The most important observable of the proposed experiment will be the single target spin asymmetry. We will here use the following notation for the target polarization:

- along z (longitudinal)

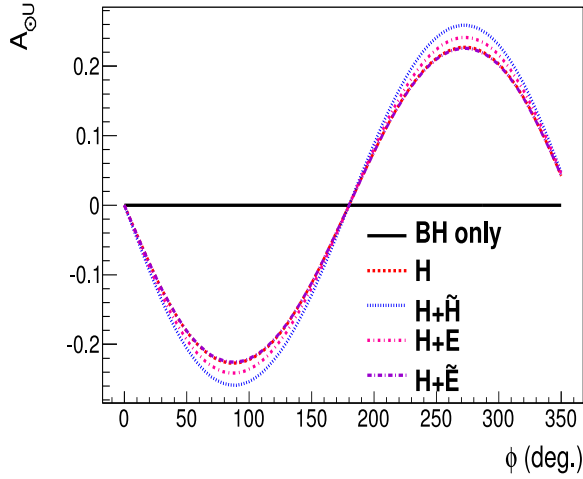


FIG. 8: The $A_{\odot U}$ for $\theta \in [45^\circ, 135^\circ]$ using different GPDs parametrizations for TCS. The calculations are done for $Q'^2 = 7 \text{ GeV}^2$, $\eta = 0.2$, $-t = 0.4 \text{ GeV}^2$.

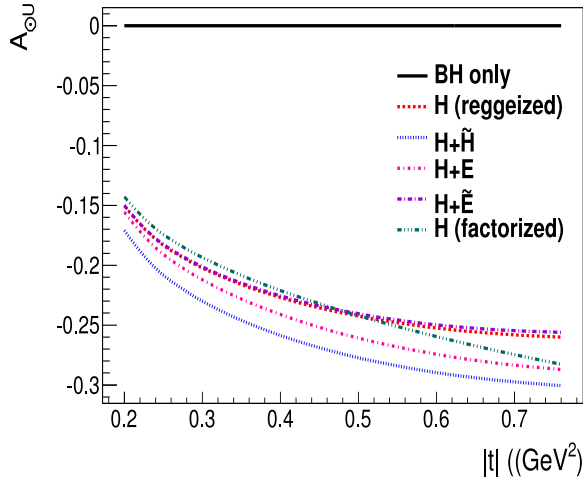


FIG. 9: The $A_{\odot U}$ asymmetry as a function of t for BH+TCS at $\eta = 0.2$, $Q'^2 = 7 \text{ GeV}^2$, $\phi = 90^\circ$ and θ integrated over $[45^\circ, 135^\circ]$. TCS is calculated with different GPDs.

- along x (transverse) the polarization vector is in the reaction plane
- along y (transverse) the polarization vector is perpendicular to the reaction plane

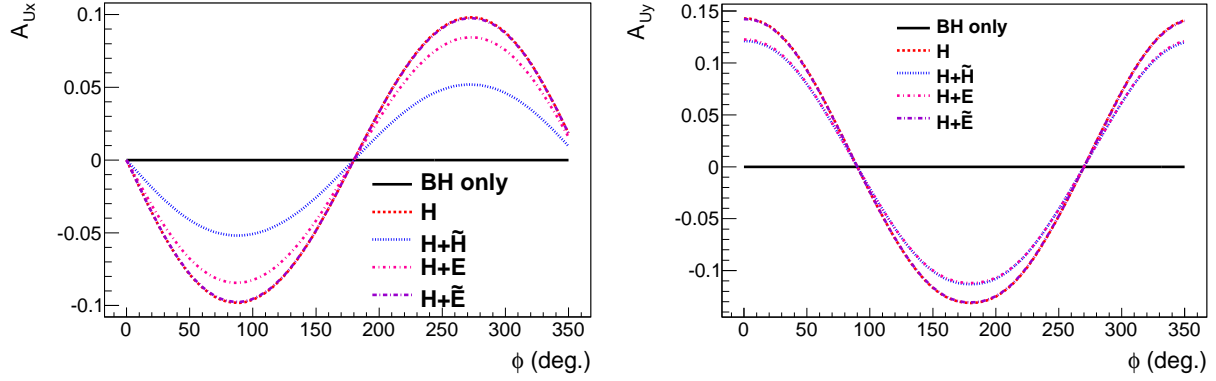


FIG. 10: TCS spin asymmetries A_{UX} (left panel), A_{UY} (right panel) as a function of ϕ for $\xi = 0.2$, $Q'^2 = 7 \text{ GeV}^2$, $-t = 0.4 \text{ GeV}^2$, and for θ integrated over $45^\circ - 135^\circ$. TCS calculated with different GPDs contributions. Figure from [8].

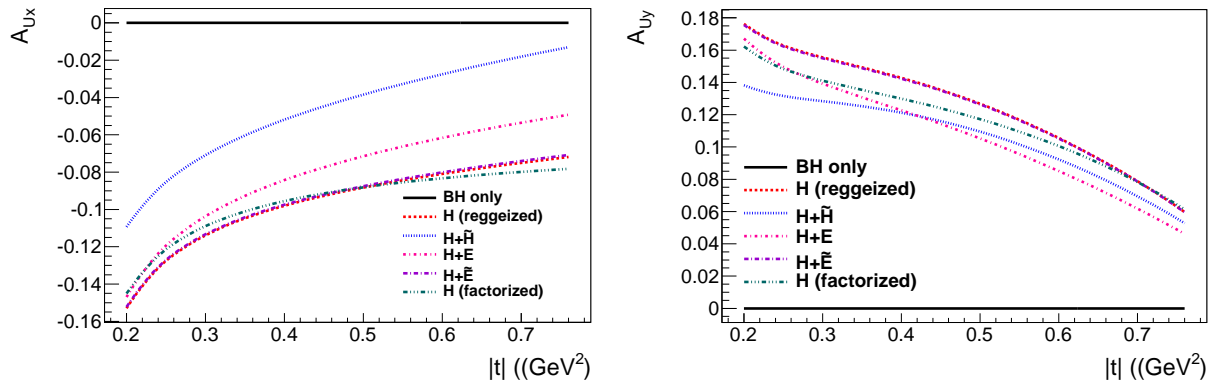


FIG. 11: TCS spin asymmetries A_{UX} (left panel), A_{UY} (right panel) as a function of $|t|$, at $\phi = 90^\circ$, 0° respectively, and for $\xi = 0.2$, $Q'^2 = 7 \text{ GeV}^2$, and θ integrated over $45^\circ - 135^\circ$. TCS calculated with different GPDs contributions. Figure from [8].

The transverse target spin asymmetries are sensitive to the imaginary part of the amplitudes and have the attractive feature that BH gives no contribution. They are therefore particularly sensitive to the TCS amplitude - and hence the GPDs. Fig. 10 shows the ϕ dependence of the 2 transverse target spin asymmetries for kinematic $\xi = 0.2$, $-t = 0.4 \text{ GeV}^2$, $Q'^2 = 7 \text{ GeV}^2$ and for $\theta \in [\frac{\pi}{4}, \frac{3\pi}{4}]$ with different scenarios of the GPD parameterization. It shows that we expect a $\sin(\phi)$ modulation for A_{Ux} and a $\cos(\phi)$ modulation for A_{Uy} . This results show important sensitivities to the GPD modeling, in particular, in addition to the GPD H , to the GPDs \tilde{H} and E . We also display the t dependence of the asymmetries at their maximal value of ϕ (90° for A_{Ux} and 0° for A_{Uy}). The maximal reachable asymmetries are up to $\sim 20\%$, and it is experimentally measurable.

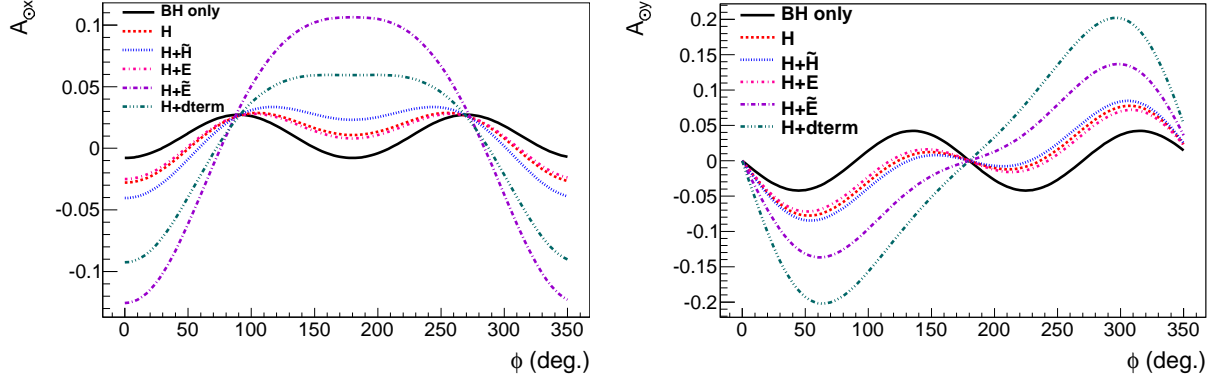


FIG. 12: Circularly polarized beam-target double spin asymmetries as a function of ϕ at $\xi = 0.2$, $t = 0.4 \text{ GeV}^2$ and $Q^2 = 7 \text{ GeV}^2$. Left column: $A_{\odot X}$, right column: $A_{\odot Y}$. In all panels θ integrated over the range 45° - 135° . Calculations are done for different GPD contributions to the TCS process. Figure from [8].

4. Double spin asymmetries: circularly polarized beam and transversely polarized target

Double spin asymmetries with a circularly polarized beam are sensitive to the real part of the amplitudes. Since BH alone gives non-zero asymmetries, they will be more challenging to extract from the measurement. These asymmetries are, however, sensitive to the GPDs, and once the experimental procedure is demonstrated, they could provide a strong constraint on the GPD fits.

This is shown on Fig. 8 where the ϕ dependence of the asymmetries $A_{\odot x}$ and $A_{\odot y}$ are presented for $\xi = 0.2$, $-t = 0.4$ et $Q^2 = 7 \text{ GeV}^2$, $\theta \in [\pi/4, 3\pi/4]$. We can distinguish a very strong sensitivity to all the GPDs, in particular to their real part. We also mention that they are very sensitive to the models. The t dependence of these asymmetries is presented on Fig. 9. We notice a change of the sign of the asymmetry for one particular model which come from the shape of the ϕ distribution (Fig. 8). The ϕ -shapes of the asymmetries are complex and very dependent on θ . In contrast to the single spin asymmetries, the ϕ -shapes are also very dependent on the specific GPDs entering the TCS process.

5. Conclusions

This proposed measurement of TCS spin asymmetries with a transversely polarized target is particularly sensitive to the imaginary part of GPDs \tilde{H} and E , and in the case of double-spin asymmetries, also the real part of the amplitude. The data will provide a strong constraint on theoretical models.

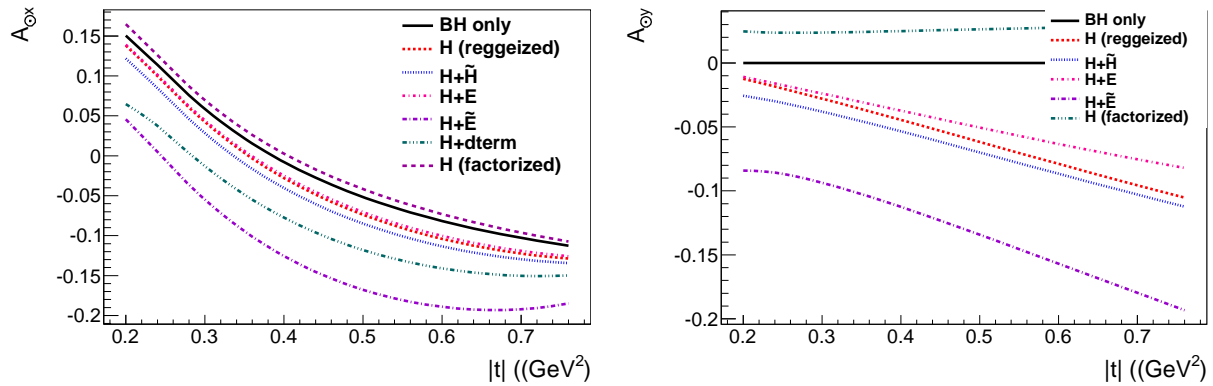


FIG. 13: Circularly polarized beam-target double spin asymmetries as a function of t . Left: $A_{\odot X}$, right: $A_{\odot Y}$. Calculations are done at the kinematics: $\xi = 0.2$, and $Q^2 = 7 \text{ GeV}^2$ and $\phi = 0^\circ$, ($A_{\odot X}$), $\phi = 90^\circ$ ($A_{\odot Y}$). θ is integrated over $45^\circ - 135^\circ$. Calculations are done with different GPD contributions. Figure from [8].

C. TCS at JLab 6 GeV

First studies of TCS using real tagged and quasi-real untagged photons were carried out at Jlab 6 GeV energy using CLAS detector [15, 16]. In these studies, rather than extracting imaginary or real part of Compton Form Factors (CFFs) or General Parton Distributions (GPDs) from the experimental data, quantity R (cosine moment of the weighted cross section normalized to the total weighted cross section), is extracted and compared to the theoretical calculations.

Several CLAS data sets with quasi-real photons ($e1 - 6$, $e1f$) have been analyzed and quantity R sensitive to TCS and BH interference amplitude extracted from asymmetry of azimuthal angular distribution.

Proposed experiment builds upon experience gained from the analysis of CLAS 6 GeV data, which has established the technique for carrying out exclusive photoproduction experiments with quasi-real photons that we propose for this experiment.

This requires the detection of all final-state particles except the scattered electron, for which the missing mass and missing transverse momentum are constrained to be very small. This technique has been successfully applied to measurements of timelike Compton scattering using the CLAS $e1-6$ and $e1f$ data sets. The results from this analysis have been documented in Ref. [15].

The results from the above analysis can be compared with an TCS analysis using the $g12$ data set [16], which was the only 6 GeV energy CLAS data set with tagged real photons.

In addition to demonstrating the feasibility of the proposed measurement, the pilot experiments at 6 GeV stimulated the development of new analysis methods. An example of this was the introduction of the cosine moment R' , evaluated within the acceptance of the detector in the

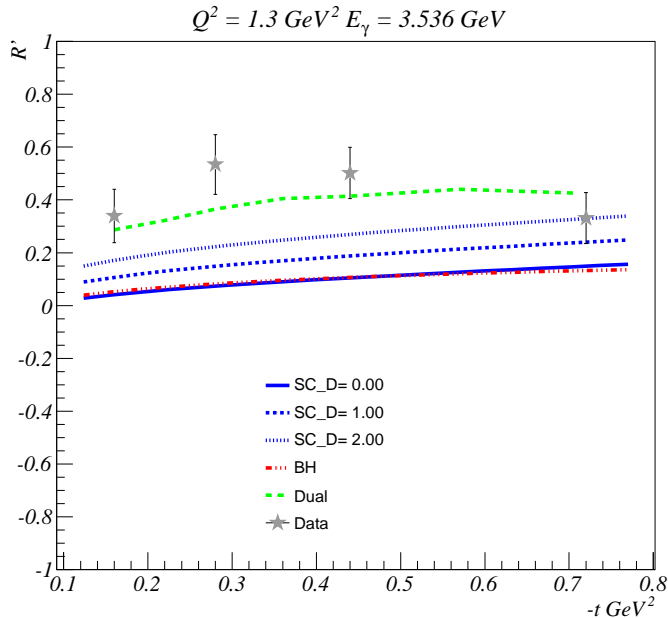


FIG. 14: The cosine moment of the weighted cross section, R' , in the CLAS acceptance compared to GPD model calculations based on the dual parametrization [17–20] (upper, green curve), and the double distribution [21] (lower, blue curves) for three weights applied to the D -term. The BH-contribution is shown in red.

$\varphi_{CM} - \theta_{CM}$ plane (the lepton c.m. angles φ and θ are defined in Fig. 4). Whereas the original definition of R implies using the integration ranges corresponding to the detector acceptance, R' adds an function $a(\theta_{CM}, \varphi_{CM})$ for a given kinematic bin.

Fig. 14 shows R' extracted from the combined e1-6 and e1f data sets for four bins in $-t$, compared with two GPD model calculations based on the dual parametrization [17–20] and double distribution [21], respectively. Results from the latter are shown with three weights for the contribution from the D -term (0, 1, and 2). Both the experimental and theoretical points shown here were evaluated at the average value for the bin, but an event-by-event approach will be adopted in the future.

However, despite the usefulness of the 6 GeV data for developing the TCS program, only the 12 GeV era will provide the required luminosity and kinematic coverage. In particular, the higher beam energy will make it possible to study a range of invariant lepton pair masses where there are no meson resonances that complicate the interpretation of the measurement. As shown in Fig. 15, only data above the ϕ mass were used for TCS analysis at 6 GeV, but at 12 GeV it will be possible to move this range above the mass of the ρ' .

During the G12 run period, an electron beam of energy 5.7 GeV went through a radiator

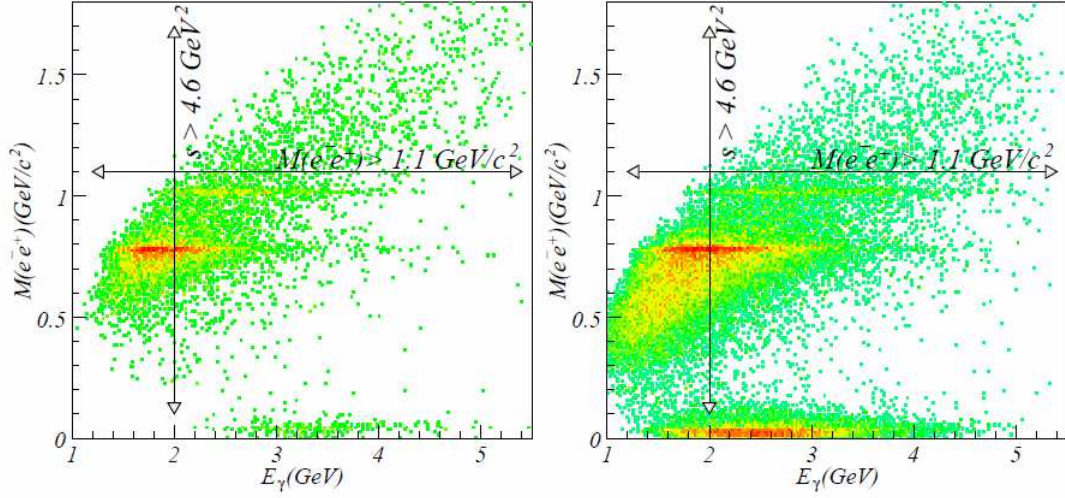


FIG. 15: e^+e^- invariant mass vs. quasi-real photon energy for the e1-6 (left) and e1f (right) data sets. Only events with M_{ee} above the ϕ mass were used for TCS analysis at 6 GeV.

(a gold foil with 10^4 radiation lengths thickness) where electrons produced real photons via bremsstrahlung with energies ranging from 1.2 to 5.4 GeV was incident on a hydrogen target and final state particles were detected by the CLAS detector.

TCS events were studied in two different topologies: requiring detected proton and not requiring detected proton in the final state. In the latter case final state protons were determined by missing mass analysis. For the first topology with requiring a detected proton, missing mass becomes $MM = M_e + M_{e^+} + M_{P_{out}} - E_\gamma - M_{P_{in}}$ while for the topology with no proton requirement missing mass can be calculated as $MM = M_e + M_{e^+} - E_\gamma - M_{P_{in}}$. In the first case missing mass distribution is populated around zero and for the second case missing mass distribution should populate around proton mass.

After accomplishing PID and background subtraction, center of mass variables θ_{CM} and ϕ_{CM} are extracted and used in the extractions of R.

Then R, the cosine moment of the weighted cross section normalized to the total weighted cross section, is extracted using the following method:

$$R = \frac{\sum_\phi \text{Cos}\phi Y_\phi}{\sum_\phi Y_\phi} \quad (9)$$

$$Y_\phi = \sum_\theta \frac{L(\theta, \phi)}{L_o(\theta)} N_\phi^\theta \frac{1}{A_{CC\phi}^\theta}$$

where θ_{CM} and ϕ_{CM} are the center of mass variables. $A_{CC\phi}^\theta$ is acceptance of the detector and N_ϕ^θ is the number of events in the corresponding θ_{CM} and ϕ_{CM} bins. θ_{CM} ($0 < \theta < 180$)

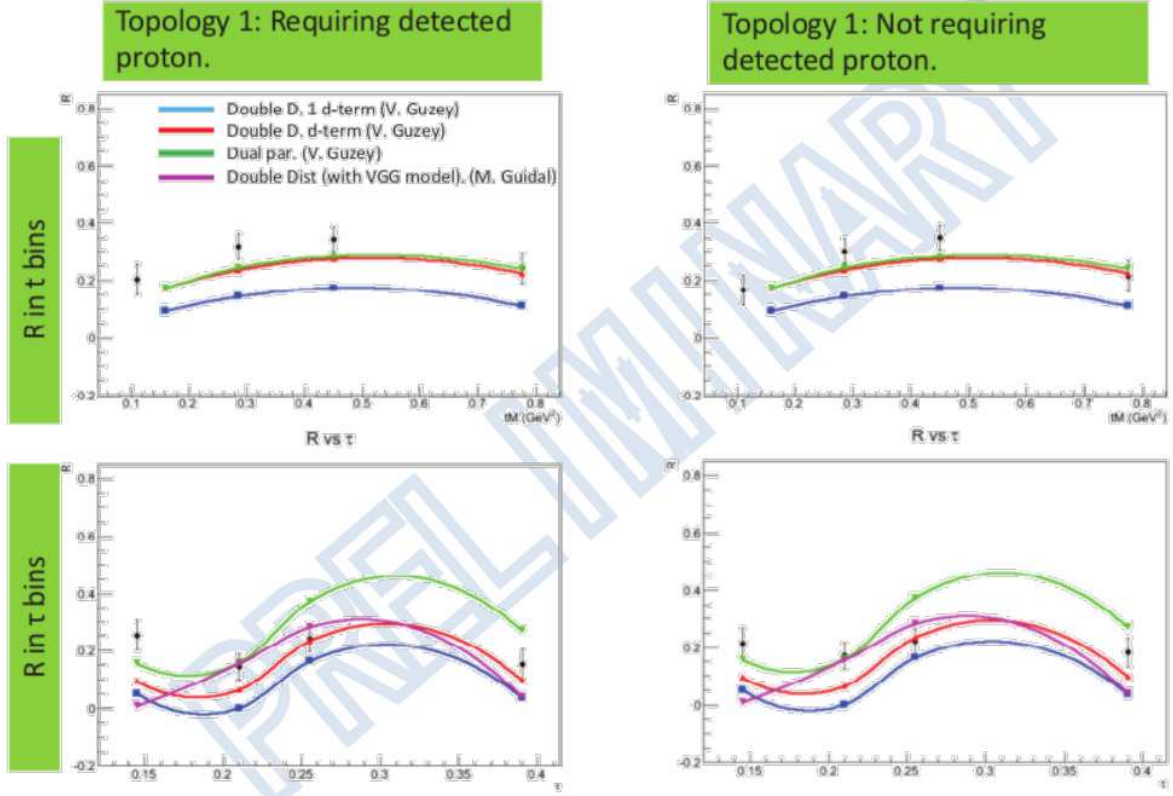


FIG. 16: Preliminary experimental results for quantity R versus t and τ , and comparisons to the theoretical calculations. Data points include statistical uncertainties only. Colored points are the theoretical calculations as shown on the figure which color correspond to which model. Points are connected by smooth curves to demonstrate the approximate behaviour between the points. (Adopted from I. Albayrak).

and ϕ_{CM} ($0 < \phi < 360$) ranges are both divided into 9 bins. R is studied in t and τ bins where both t and τ coverage are divided into 4 bins such that each bin has similar number of events.

Preliminary results from Jlab CLAS $g12$ experiment performed with clean real photon beam are shown for both R versus t and R versus τ extracted in two topologies.

The following steps were carried out before extracting the final results:

- Vertex time analysis,
- ee^+ invariant mass analysis,
- Extracting TCS kinematic variables,

- Acceptance calculations and integrations ranges
- Extracting R.

There is no direct way of estimating statistical uncertainties from data itself, since only one number is extracted per bin from the whole data for the measured quantity R, four numbers in total for four bins in τ or t . Therefore the following procedure is used to determine the statistical uncertainties. The uncertainties of the yields are assumed to have Gaussian shapes and a large number of pseudo R data (10^5) are generated with randomly generated yields within the assumed Gaussian statistical uncertainties. Then the obtained distribution of pseudo R data is fitted with a Gaussian function and the standard deviation of the fit is used as the statistical uncertainty for the R in the corresponding t or τ bin.

There are mainly three sources of systematical uncertainties in this analysis. These are bins sizes when integrating over θ and ϕ , calculation of lepton propagator term, the determination of the integration range in θ , and determination of π background rejection.

Theoretical calculations are not describing simultaneously t and τ dependence (see Fig. 16). This is the first time study of τ dependence of R which is important, since theoretical GPD calculations can demonstrate significant differences over τ .

CLAS 6 GeV data demonstrated the general feasibility to access GPDs through experimental studies of Timelike Compton Scattering (TCS).

The analysis of the g12 data is still ongoing, but preliminary results seems to be in line with what was obtained with the quasi-real photon technique. The tagged-photon beam will also make it possible to do an independent determination of the photon flux, and offer an opportunity to explore event topologies with only two out of the three final-state particles detected.

3. EXPERIMENTAL SETUP

A. Lepton detectors

The determination of the kinematic variables Q'^2 , ξ and τ depends solely on the accuracy of reconstruction of the lepton energy and angle. Leptons (e^+ and e^-) in the experiment will be detected and identified by measuring their energies, and coordinates (X and Y) in a pair of electro-magnetic calorimeters.

The calorimeters are thought to be clone of the shower counter for the projected Neutral Particle Spectrometer. The basic concept for the NPS is a highly segmented electro-magnetic calorimeter preceded by a compact sweeping magnet. Experiments with NPS require detection of neutral particles with energies ranging between 0.5-7.6 GeV with good energy resolution ($\sim 2\%$), and good coordinate and angular resolution of 0.5-0.75 mrad, the latter is comparable to the

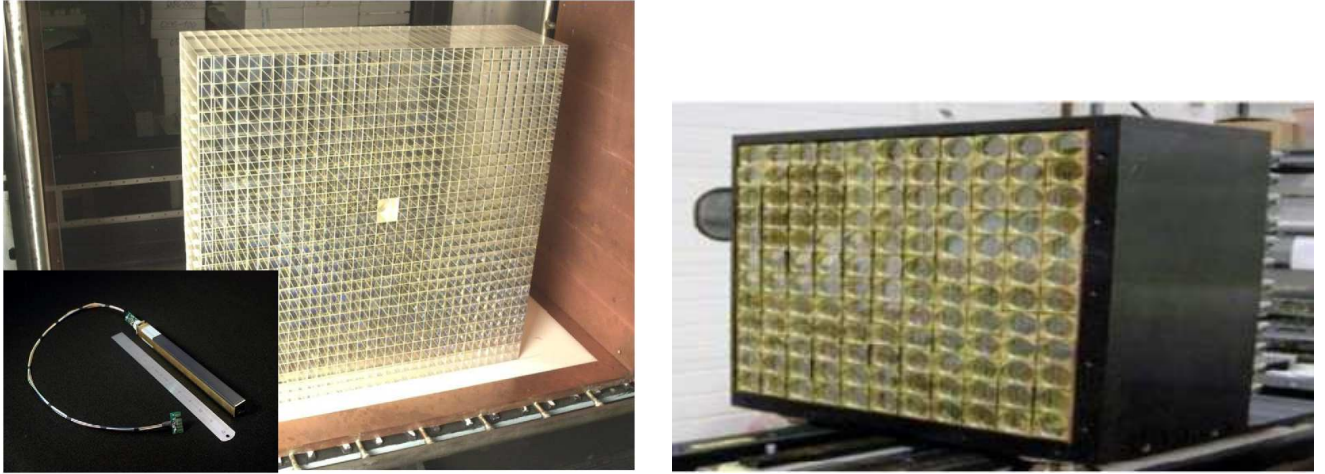


FIG. 17: Left: $2.05 \times 2.05 \times 18\text{cm}^3$ PbWO_4 crystals used in the high resolution part (HYCAL) of Hall B PrimEx experiment calorimeter [22]. Right: the Hall A DVCS calorimeter made of $3 \times 18\text{cm}^3$ PbF_2 crystals.

resolutions of the focusing spectrometers in Hall C. The NPS can take advantage of existing PbWO_4 and/or PbF_2 crystals, that were used for the PRIMEX and PRIMEX-II experiments in Hall B and the DVCS experiments in Hall A (see Fig 17). The new active divider design of the PMT bases provides a linear response up to high rates of ~ 1 MHz. More information about the NPS and design studies can be found in reference [23].

In the construction of the Primex PbWO_4 and Hall A DVCS PbF_2 detectors the components were carefully characterized, and calibration procedures were developed that can be adapted to this project. Experience with the HYCAL yielded energy and coordinate resolutions of $\sigma/E = 1.3\%$ and $\sigma_x \sim 1.28\text{-}2.10$ mm at a neutral-pion energy of 5 GeV, giving an invariant mass distribution with a width of $2.3 \text{ MeV}/c^2$ (see Fig, 18).

The size of the TCS lepton detectors is driven by required angular acceptance and distance to the target. Restricted by the target setup angular acceptance is $\pm 17^\circ$ in horizontal plane and $\pm 26.5^\circ$ in vertical plane (see Section 3 D). In addition, the beam pipe restricts scattering angles to greater than 6° . Taken into account vertical deflections of the particles to be detected in the sideways magnetic field of the target, we consider positioning the lepton detectors above and below the beam pipe, at 0° of azimuthal angle.

Reasonable sizes for the detectors can be obtained by positioning them at a distance ~ 1.5 m from the target. This implies $92 \times 60\text{cm}^2$ of active area, for the angular acceptances $\pm 17^\circ$

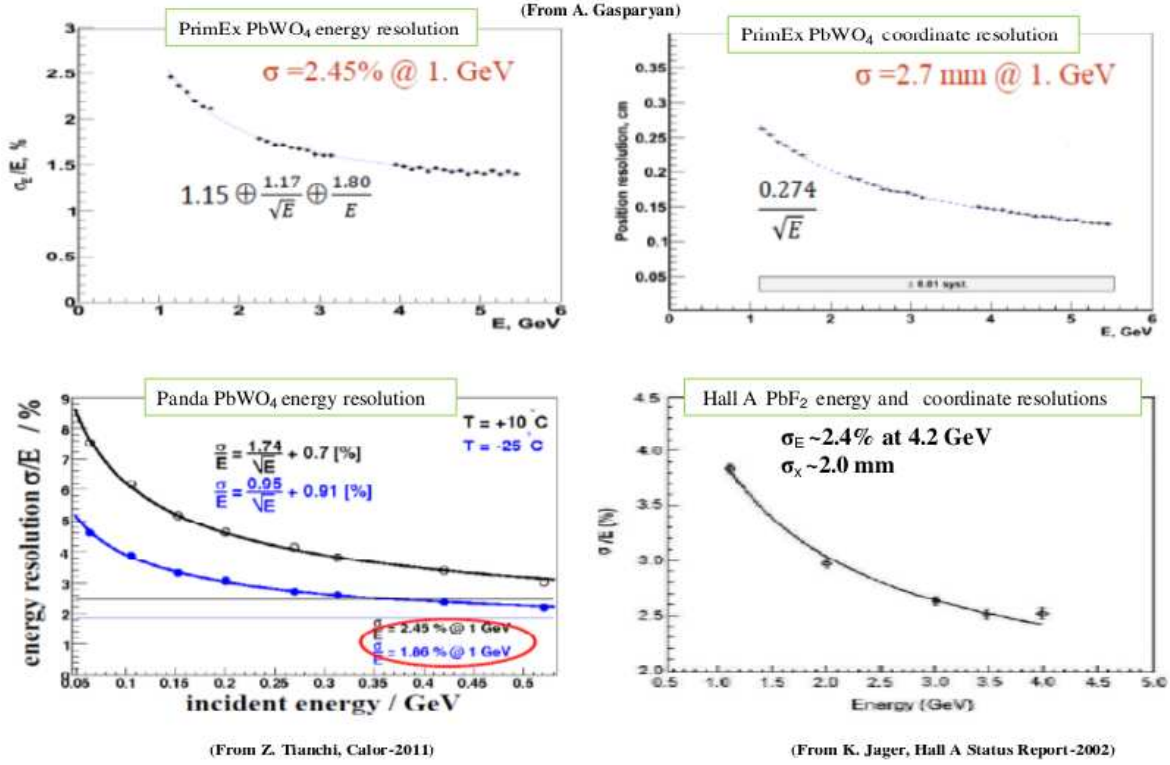


FIG. 18: Energy and coordinate resolutions of PbWO_4 and PbF_2 crystals based calorimeters.

horizontally and $\pm 20.5^\circ$ vertically. Assuming PbWO crystals of $2.05 \times 2.05 \text{ cm}^2$ cross section for construction (like in the HYPAL part of the PrimEx detector), the number of modules would be ~ 1400 for each detector.

B. Detection of recoil protons

The determination of the $-t$ and its resolution depends on the accuracy of reconstruction of the recoil proton four momentum. The design requirements for the proton detectors are defined by kinematics, required accuracy, available space and cost, as well as by the expected background conditions. The proposed two recoil detectors will be located just before the lepton detectors and will cover all horizontal (θ) and vertical (ϕ) angular area allowed by the polarized target (θ from -17° to $+17^\circ$, and ϕ from 6° to 26.5° , and from -6° to 26.5°). As lepton detectors, they will be located symmetrically up and down relative to the beam-line.

The proton detectors will have hodoscopic construction. Each hodoscope will consist of X and Y planes and will cover effective area of $\sim 90 \times 60 \text{ cm}^2$. At 1.5 m distance from the target they will cover $\sim 300 \text{ msr}$ acceptance for recoil protons.

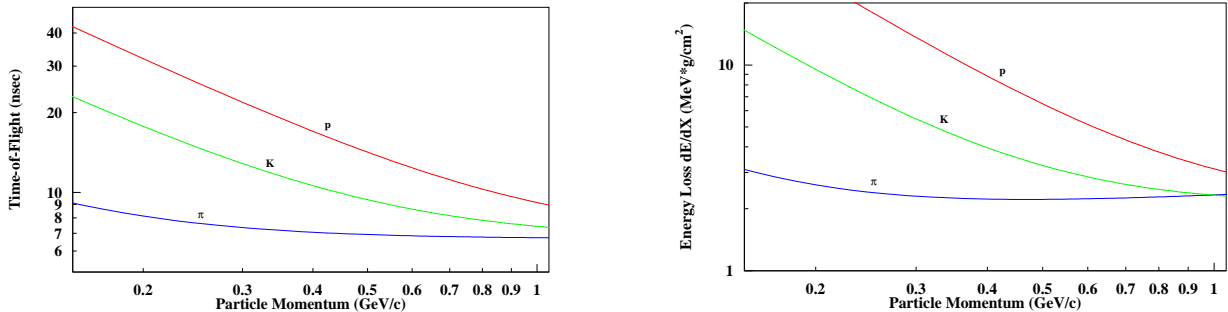


FIG. 19: Proton PID by TOF and dE/dx in the Recoil Proton Detector. The graphs show time-of-flight and ionization energy losses versus momentum for pions, kaons and protons.

Scintillator bars of 1 cm thickness can be used in construction of the hodoscopes. As momenta of detected leptons are above 1 GeV, traversing the 2 cm thick scintillator material will not affect much performance of the lepton shower counters.

The detected proton momenta will be within $0.3 - 1.5$ GeV/c range, with bulk of statistics between 0.4 and 0.8 GeV/c. By use of time and amplitude information from the scintillation counters, with a time resolution ~ 200 ps and flight path of about 100 cm (distance between a tracker at the scattering chamber window and the hodoscopes), and good amplitude resolution, protons with momenta up to 1.5 GeV can be identified by the TOF and dE/dx , as shown in Fig. 19. The coordinate information (X and Y hit bars) will be used for reconstruction of the proton momentum and recoil angles (θ_p , ϕ_p).

C. Tracker

Two sets of identical tracking detectors located at minimal distance from the target, just outside the scattering chamber windows, below and above the downstream beam-line will be used in experiment. This would be the simplest and cost-effective way to get additional and independent information on position and energy loss of the reaction products.

The Trackers will have effective area of $\sim 30 \times 20$ cm² and will cover horizontal angle $\pm 17^\circ$ and vertical angle from 6° to 26.5° and from -6° to -26.5° , the full available angular acceptance for protons and leptons.

Each Tracker will consist of X and Y planes allowing to determine X and Y coordinates of the outgoing leptons and proton with accuracy of $\sigma \sim 0.9$ mm. The neighboring fibers in both layers will be slightly overlapped to exclude passage of particles without detection. This will require ~ 300 fibers for each tracker. The multi-anode phototubes (64 channel Hamamatsu) will be used for read-out of the large number of scintillating fibers.

The two layers of the Trackers will be used for reconstruction of particle trajectory and as a start-time for TOF system. In addition to providing space points, the scintillating fiber tracker may work for particle identification as well.

The target magnetic field at the Trackers (~ 50 cm from target) is ~ 1.5 kG. So, to minimize field effects light from both sides of the tracker will be transported to 64 channel PMTs by ~ 2.5 m Wave-Length-Shifter (as it was done in SANE experiment [25]) allocated in an area where magnetic field is below ~ 100 G. The Multi-Anode PMTs (MAPMTs) have been tested to work without any problem with longitudinal magnetic fields up to 400 G.

Similar technique was implemented in the HERMES Recoil detector where identification of protons and pions in the momentum range from 250 MeV/c to 1500 MeV/c required [24, 26]. The signals from the scintillating fibers were collected using MAPMTs Hamamatsu H-7548. The energy response (number of photoelectrons equivalent to particle energy loss dE/dx) of fibers (1 mm diameter scintillating fiber Kuraray SCSF-78) to protons and pions of the various momenta is shown in Fig. 20.

A clear separation between protons and pions using only dE/dx is possible in the range $250 \text{ MeV} < P < 450 \text{ MeV}$. At higher momentum range (up to ~ 1500 MeV) π/p separation is possible by combining dE/dx information from the scintillating fibers and TOF system (see Fig. 21).

During normal operation, the fibers of the Tracker will be exposed to radiation doses of the order of 50-100 Gy/yr. The Kuraray fibers are developed for improved radiation resistance. They had previously been investigated in terms of radiation hardness for the development of a hodoscope for the COMPASS experiment [27], for the possible use in the inner tracker of HERA-B [28], and for the tracking system of ATLAS [29]. These studies showed that these plastic scintillating fibers should not deteriorate significantly at the accumulated doses of ~ 100 Gy/yr.

D. Polarized Target

Hall C has a long and successful experience with the use of solid polarized targets, starting in 1998 with the first run of E93-026[30] designed to measure the electric form factor of the neutron. This was followed by its second run in 2001 and immediately by the Resonance Spin Structure experiment, E01-006[31] in 2002 and by the Spin Asymmetries Experiment on the

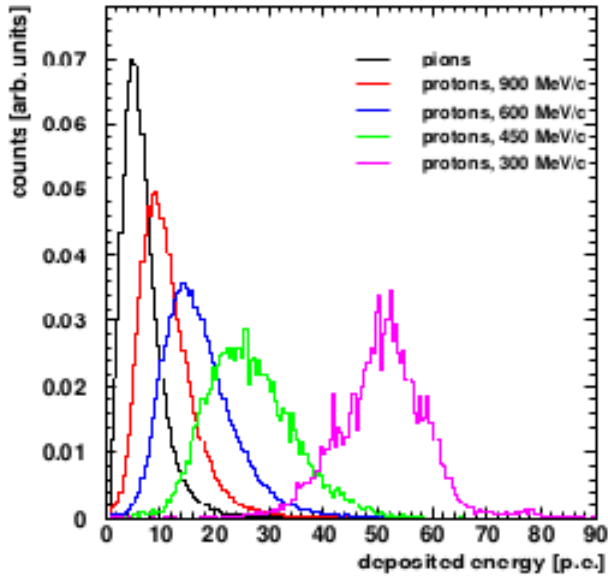


FIG. 20: Energy response of tracker fibers for pions and protons of various momenta. The picture adopted from Ref. [24].

Nucleon (SANE)[32] in 2009.

These targets exploit a technique called Dynamic Nuclear Polarization (DNP) in which polarization is transferred from unpaired electrons in a dilute concentration of paramagnetic centers (introduced via irradiation at 80K or by chemical doping). At 5 T and 1K the thermal equilibrium of both species (proton and electron) is determined solely by Boltzmann statistics and can be written as $P = \tanh \frac{\mu B}{kT}$. The TE polarization of the electron under these conditions is 99.8% while the proton is 0.51%, the difference due solely to the size of their respective magnetic moments. The dipole-dipole interaction between the nucleus and the electron spins leads to hyperfine splitting. By applying a RF field with a frequency very close to the electron spin resonance frequency (about 140 GHz at 5.0 Tesla), the high electron polarization (due to the large electron magnetic moment) can be transferred to the proton.

In the case of the proton, the direct polarization enhancement is achieved by driving the transition from the ground state of $e_{\frac{1}{2}}p_{\frac{1}{2}}$ to the state $e_{\frac{1}{2}}p_{\frac{3}{2}}$ by applying microwaves with frequency around 139.914 GHz. See Figure 22.

The schematic view of the polarized target and the lower part of the target insert are shown in Fig. 23. The target magnet is a pair of superconducting Helmholtz coils that when driven at 77 A produce a magnetic field of 5 Tesla. The coils have a 20 cm central bore, 100° opening angle and 8 cm of coil split. The field is uniform to 10^{-4} over 3 cm diameter right

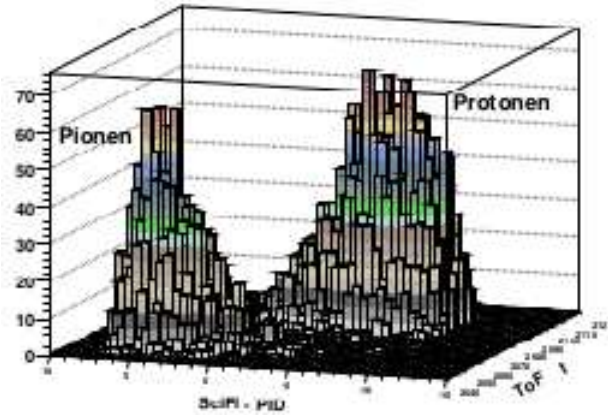


FIG. 21: Particle identification with the SciFi in HERMES Recoil detector tracker obtained at the GSI test beam. The picture adopted from Ref. [24].

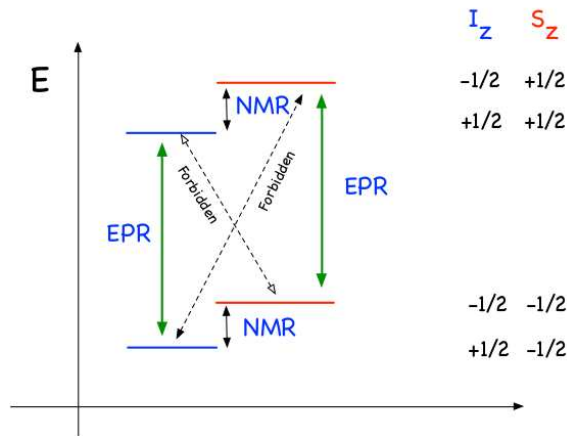


FIG. 22: Transitions driven by GHz microwaves in the DNP process

cylinder.

To provide transverse polarization of the target needed in this measurement, the target assembly will be rotated by 90° around vertical axis. Restricted by the magnet coils and scattering chamber window, the angular acceptance in this configuration will span $\pm 17^\circ$ horizontally and $\pm 26.5^\circ$ vertically.

The target magnetic field direction has been found to be coincident with the geometric axis of the coils and is known to 0.1° [33]. The target is cooled by a 4He evaporation refrigerator placed vertically in the center bore of the magnet. It is contained in a separate vacuum shield (see Fig. 23). The target material is held in cups at the the end of the target insert which can

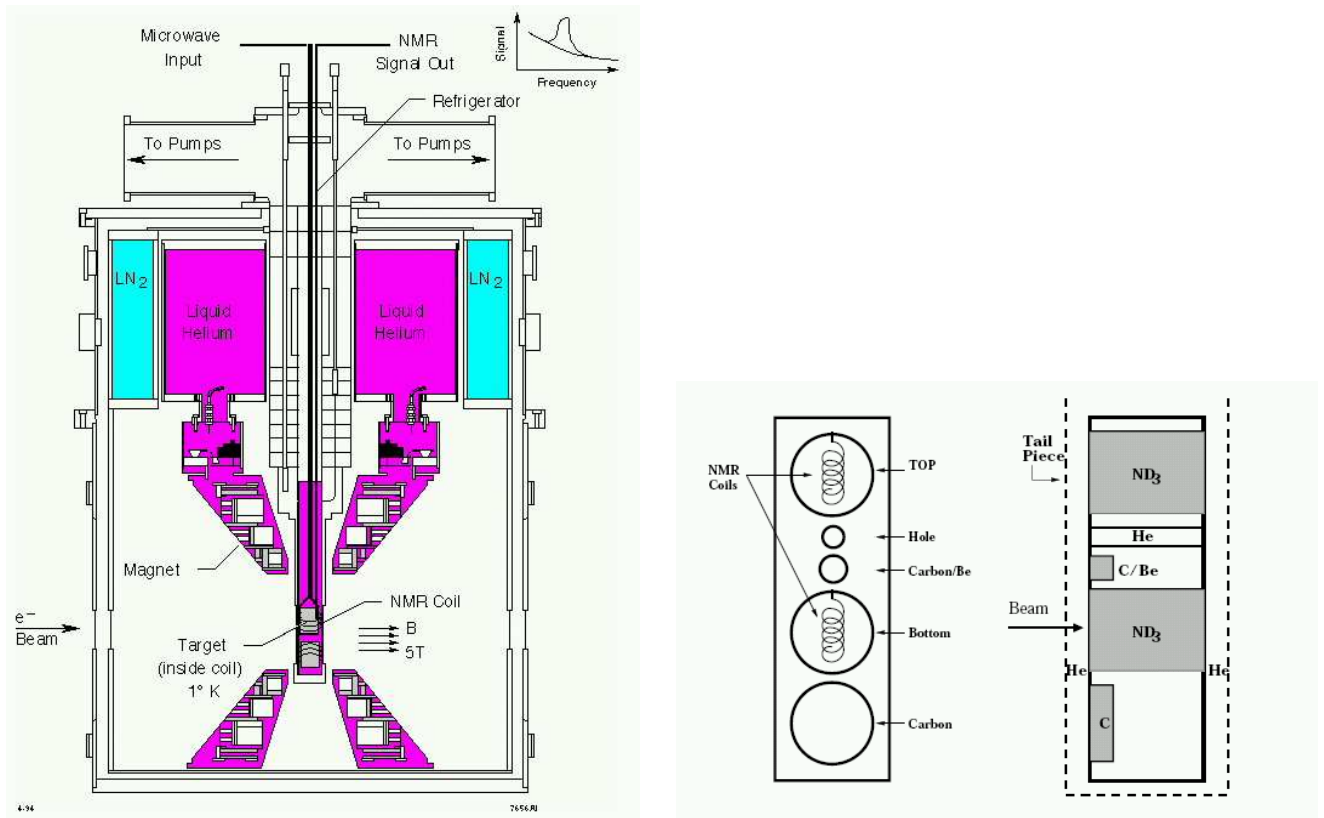


FIG. 23: The UVA polarized target used in Hall C experiments. Left: Cross section view of the target. Right: A schematic drawing of the lower part of the target insert. The dashed line represents the tail piece which contained liquid helium during data taking.

carry up to 5 targets: a top and bottom NH_3 , an empty target and 2 solid targets (C or Be).

The microwaves are generated by an Extended Interaction Oscillator tube (Manufactured by CPI, Canada) which has a maximum power of ~ 20 W with approximately 1 W delivered to the target sample. $^{15}NH_3$ is chosen as the target material because of its high polarizability, large polarizable nucleon content and resistance to radiation damage.

The target polarization is measured via NMR using the Liverpool Q-meter in which the magnitude of polarization is linearly related with the voltage of the phase sensitive detector: $P = K \cdot S$, and K is a calibration constant. The calibration constant K is determined at thermal equilibrium. A series of NMR signal area measurements are made and averaged to obtain the calibration constant. They are typically done with each load of target material and as many

time as is possible during the run, especially after anneals.

The target material consists of 1-3 mm diameter granules of NH_3 , immersed a 4He bath inside the target cavity. The packing fraction is the fraction of target cell volume filled by target material (NH_3), the rest of the cell being filled with liquid 4He . The packing fraction is important for the simulation of the scattering cross sections and for the determination of the dilution factor. The dilution factor, f , is defined as the fraction of events originating from polarized hydrogen.

The electron beam causes a decay of polarization due to radiation damage caused by the build up of 'bad' paramagnetic centers. which allow more relaxation paths through the forbidden transitions. The decay of polarization continue until the measurement time for a given accuracy becomes unacceptable. In ${}^{14}NH_3$, polarization can drop from above 80% to 60% after a dose of approximately 2 to 4 Pe^-/cm^2 , where Pe^- indicates 10^{15} electrons. For experiments using 100 nA beam current like this one, this can occur in about 8 hours. Fortunately, the process of annealing recombine the paramagnetic centers and restore polarization. To anneal the target material is moved out of the beam and the polarizing microwave radiation and is heated to between 70-100 K for between 10 and 60 minutes.

The detailed information about polarized target subsystems, technique of operation and experimental measurements can be found in Ref. [34, 35] and the UVa target group web server Ref.[36].

4. EXPERIMENT KINEMATICS AND PROJECTED RESULTS

In this section we describe the kinematics, acceptances, analysis methods and projected uncertainties of proposed experiment. We propose to study quasi-real photoproduction of lepton pairs, $ep \rightarrow l^+l^-p'(e')$, in a wide range of kinematics. The analysis will use the quasi-real photoproduction reaction:

$$ep \rightarrow e^+e^-p'(e') \quad (10)$$

where the initial electron (e') scatters at a small angle ($\sim 0^\circ$), and escapes detectors. In Eq. (10), e^+e^- is the produced lepton pair, and p' is the recoil proton.

The final state contains two leptons and a proton, which will provide a coincidence trigger. To suppress background from two-pion photoproduction, the trigger has to contain the two leptons energy cut, at least on the level of 300 MeV.

The exclusivity of the reaction is ensured by detecting all final-state particles, e^+e^-p and cutting on the missing-particle kinematics (transverse momentum and missing mass), in a similar manner as in the TCS analysis of the CLAS 6 GeV data [15].

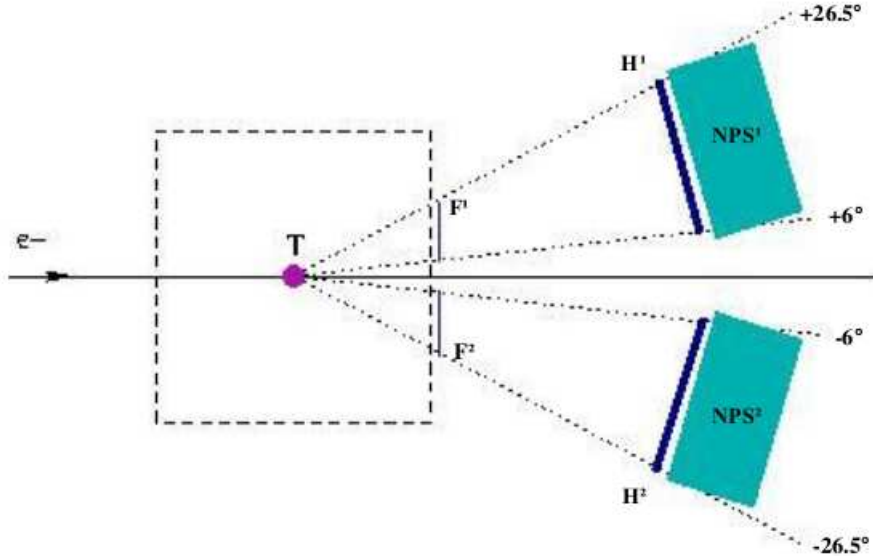


FIG. 24: Schematic sideview of experimental setup. NPS type electromagnetic calorimeters and recoil proton detectors span from $+6^\circ$ to $+26.5^\circ$ and from -6° to -26.5° relative to the beam-line. (Angular coverage in horizontal plane for both arms is $\pm 17^\circ$).

This experiment will use 11 GeV energy unpolarized electron beam incident on transversely polarized protons (solid ammonia NH_3) at luminosities up to $L = 10^{35} \text{ cm}^{-2} \text{ sec}^{-1}$.

The combination of three groups of the detectors will allow for detecting the lepton pair and recoil protons in coincidence. A pair of electromagnetic NPS-type calorimeters will be used for detection of leptons, determination of their energies, tracking (in combination with tracker) and for e/π separation and a pair of recoil detectors will be used to detect protons. These detectors will be combined with a tracker, and Hall C basic electronics and DAQ. The experimental setup is shown in Fig. 24.

We assume that the NPS-type calorimeters and recoil hodoscope systems will be positioned at angles of from 6° to 26.5° and from -6° to -26.5° up and down relative to beam-line, covering $\pm 17^\circ$ in horizontal plane. The proposed design characteristics of the detectors are presented in Table I.

A. Kinematics of proposed experiment

The simulations of the detector for the proposed measurements used an 11 GeV electron beam and a 3 cm long solid ammonia target. Exclusive e^+e^-p events, with invariant masses of the lepton pairs in the resonance-free region between 2 and 3 GeV, were generated over a

Parameters	Calorimeters	Hodoscope	Tracker
range in θ	$\pm 17^\circ$	$\pm 17^\circ$	$\pm 17^\circ$
range in ϕ	$6^\circ - 26.5^\circ$ $-6^\circ - -26.5^\circ$	$6^\circ - 26.5^\circ$ $-6^\circ - -26.5^\circ$	$6^\circ - 26.5^\circ$ $-6^\circ - -26.5^\circ$
$\delta\theta$	< 5 mr	$< 1^\circ$	~ 2 mr
$\delta\phi$	< 5 mr	$< 1^\circ$	~ 2 mr
Energy resolution	$\sim 2\%/\sqrt{E}$	$\sim 10\%$	$\sim 10\%$
Time resolution	< 100 ps	< 100 ps	~ 100 ps
PID:			
e/ π	~ 0.01	...	
π/p	~ 0.1	

TABLE I: Proposed characteristics of the TCS-setup.

wide range of kinematics by using the standalone event generator genTCS [37]. Both quasi-real photons from electron scattering, according to the equivalent photon approximation (EPA) [38], and real photons from Bremsstrahlung [39] on the target were included. Each event was weighted by the Bethe-Heitler (BH) cross section from Ref. [6].

B. Acceptance

The genTCS generated lepton and proton tracks were traced through the magnetic field of the target, then scattering chamber window up to the detectors at 1.5 m distance from target. As target field is oriented sideways relative to the beam direction, the tracks are deflected up and down. The track bending happens close to the target, for the field being localized within ~ 15 cm space at target. The fringe fields do not affect significantly tracks. The high momentum electrons deflect by only $\sim 2^\circ$. While for protons, with momenta from 0.3 to 1.5 GeV/c the bending angle is $\sim 15^\circ - 20^\circ$, typically, and may reach 75° .

The angular acceptance is limited by the magnet poles and the closely matching to them chamber window: $\pm 17^\circ$ horizontally and $\pm 26.5^\circ$ vertically. The beam pipe downstream the target chamber poses small angle limit of $\pm 6^\circ$. Hence positions and sizes of the lepton and proton detectors, and the tracker as well are chosen to match outgoing track directions.

Distributions of the main kinematic quantities for the TCS events within geometric acceptances of the detectors are shown in Fig. 25.

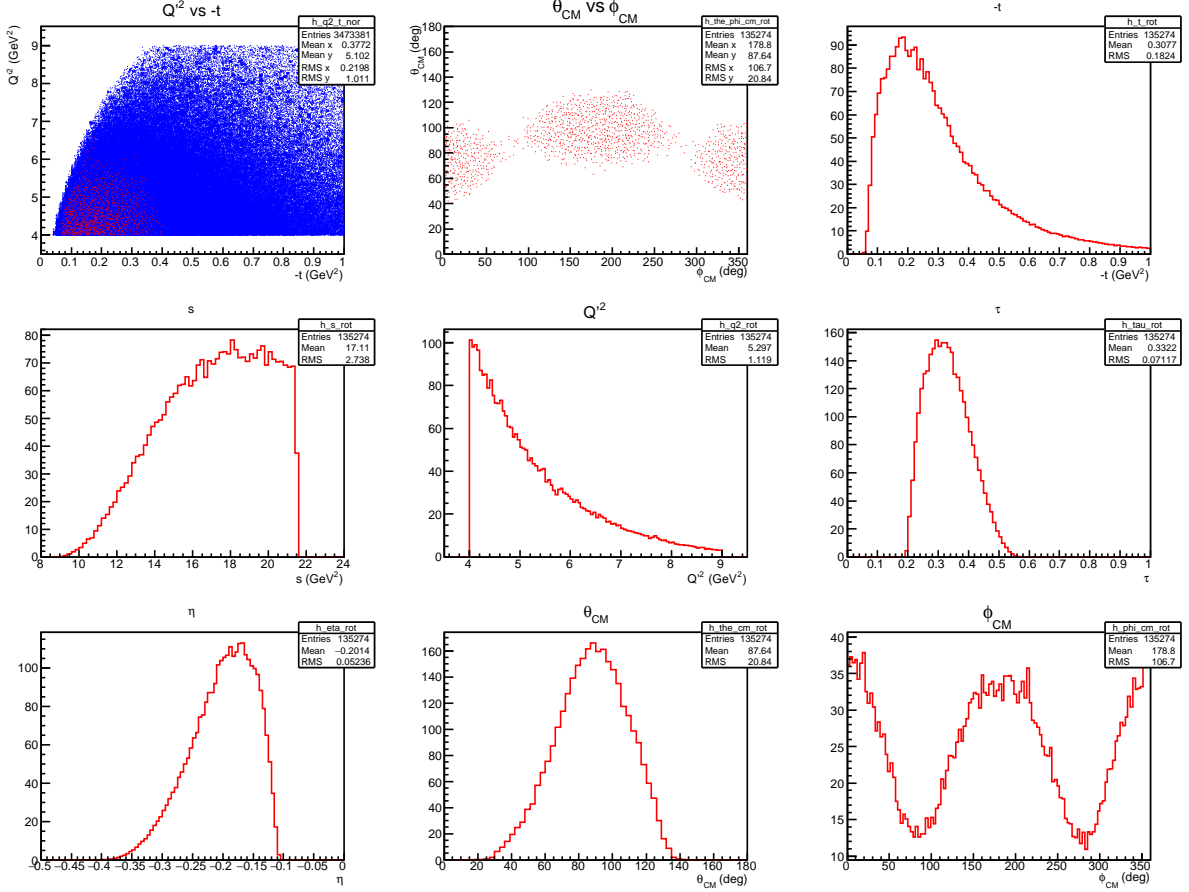
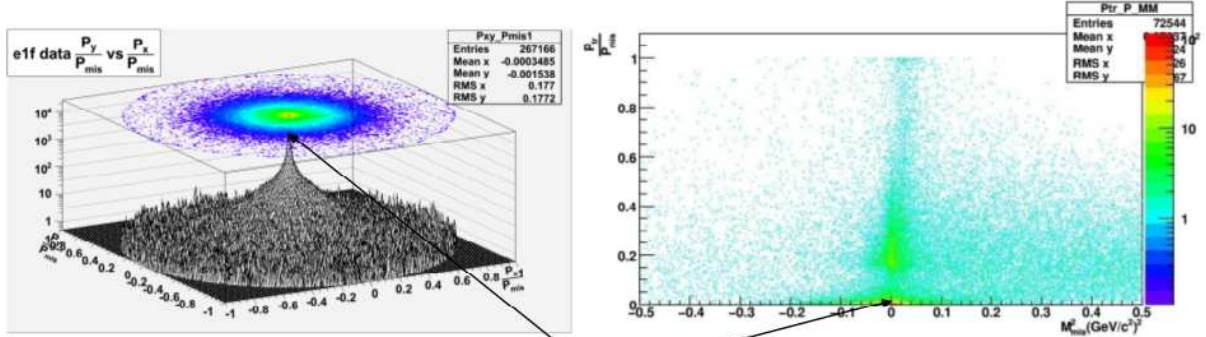


FIG. 25: Distributions of the TCS kinematic variables for 11 GeV energy incident electrons after detector acceptance cuts. From top to bottom and left to right are: Q'^2 versus $-t$ and θ_{CM} versus ϕ_{CM} , $-t$, s , Q'^2 , τ , η , θ_{CM} and ϕ_{CM} distributions. In the first panel generated events are in blue, accepted events are in red.

C. TCS Analysis

Time-like Compton scattering (TCS) is the photoproduction of dileptons. In this experiment we will use data when electron scatters at very small angle ($\sim 0^\circ$). In this case, virtuality of the emitted photon defined as $q^2 = (q - q')^2$, where $q(q')$ is four momentum vector of initial (scattered) electron, will be very small ($q^2 \sim 0$). Events produced in such scattering correspond to quasi-real photoproduction. So, we will use quasi-real photoproduction of ee^+ pairs for TCS analysis.

Since in TCS reaction final γ^* and recoil proton are produced back-to-back in c.m. frame, the inelastic events most of time will have a transverse momentum component with respect to



X – is identified as an electron scattered at 0 degrees, $Q^2 < 0.01$ (GeV/c)² and $|M_x^2| < 0.1$ (GeV)²

FIG. 26: Missing momentum and missing mass distribution for the events from quasi-real photoproduction reaction $e + p \rightarrow e^+ + e^- + p(e')$, observed in CLAS $e1f$ data analysis. Cuts $Q^2 < 0.01$ GeV² and $|M_x^2| < 0.1$ GeV² have been applied for selection TCS events. Figure adopted from Ref. [15].

the direction of the recoil momentum, and thus violate coplanarity with the reaction plane. This can be used to minimize contributions from the background reactions. A selection in coplanarity and transverse momentum exploits the fact that the momentum vector of the recoil proton has to coincide with the reaction plane.

From whole data set will selected only events which have exactly pair of leptons and one proton in final state. Then X and Y components of the missing momentum (P_X^{miss} and P_Y^{miss}) normalized to the missing momentum (P^{miss}) and missing mass square (MM^2) of the e^+e^-p system will calculate.

The strong enhancement of events at **zero** in distribution $\frac{P_X^{miss}}{P^{miss}}$ over $\frac{P_Y^{miss}}{P^{miss}}$, and missing mass distribution will corresponds to TCS events.

In order to select TCS events in reaction $\gamma^*p \rightarrow e^+e^-p$ cuts on the transverse components of the missing momentum and the missing momentum will be applied.

As an example, in Fig. 26 are shown distributions of the Y component of the missing momentum versus X component of the missing momentum, and missing mass distribution for selected e^+e^-p events from reaction $e + p \rightarrow e^+ + e^- + p(e')$.

D. Projections

The projections have been made for 30 days of running (assuming full time running) with a luminosity of 10^{35} cm⁻²s⁻¹ on a 3 cm long polarized solid ammonia target.

Events are weighted according to Ref. [8] using GPDs parameterization from VGG model [12]. The event generator (developed by M. Boer) generates flat distributions in 5-dimensional phase space (E_γ , t , Q'^2 , θ and ϕ). For each event the generator returns a weight for TCS+BH, TCS only and BH only. It also returns single and double circularly or linearly polarized beam and/or linearly or transversely polarized target asymmetries for given kinematic. It generates a photon beam or an electron beam (user choice) which is projected on a target at rest. If the electron beam option is turned on, the quasi-real photon flux is calculated according to [38] and the Bremsstrahlung photon flux is calculated according to [39]. We assume a maximal Q^2 virtuality for the "quasi-real photon" $Q^2 < 0.3$. Event kinematics is corrected by a $Q^2 \neq 0$ factor compared to the original kinematics of TCS.

1. Counting rates

The counting rates are estimated in the phase space divided into 4 two-dimensional bins in ξ, t (Fig. 27), 2 bins in $-t$ ($[.1, .35]$ GeV^2 and $[.35, 1]$ GeV^2), and 14 bins in ϕ (from 0 to 2π). The bin limits are given in table II. The estimates for counting rates are presented in fig. 28.

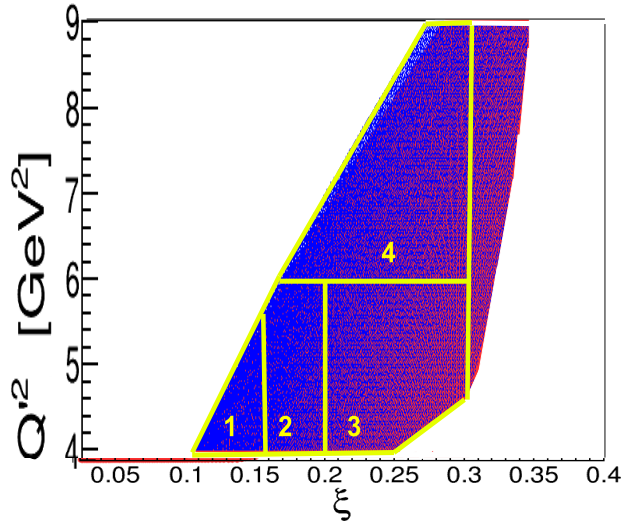


FIG. 27: Projection of the phase space for Hall C TCS measurements onto (ξ, Q'^2) plane. The four bins in table II are shown.

N	ξ limits	Q'^2 limits (GeV ²)	$-t$ limits (GeV ²)
1.0	0.10, 0.15	4, 6	0.1, 0.35
2.0	0.15, 0.20	4, 6	0.1, 0.35
2.1	0.15, 0.20	4, 6	0.35, 1
3.0	0.20, 0.30	4, 6	0.1, 0.35
3.1	0.20, 0.30	4, 6	0.35, 1
4.0	0.15, 0.30	6, 9	0.1, 0.35
4.1	0.15, 0.30	6, 9	0.35, 1

TABLE II: Proposed binning for the Hall C TCS analysis. The values in columns 3, 4 and 5 are the edges of the bins. The first column indicates separated by period (ξ, Q'^2) and $-t$ bin numbers.

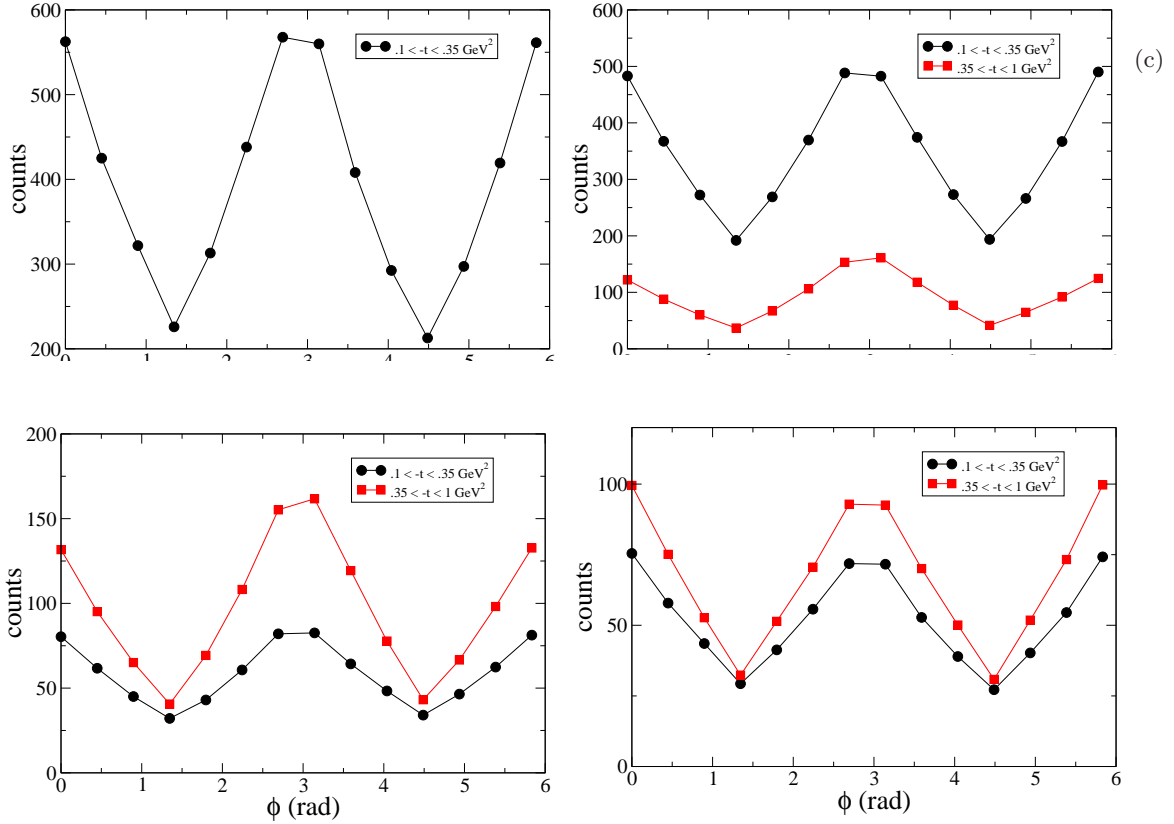


FIG. 28: Expected counting rates in 14 ϕ bins, for the 2 bins in t (black and red curves and symbols) and for the 4 (ξ, Q'^2) bins (4 panels).

5. SYSTEMATIC UNCERTAINTIES

The two main sources of systematic uncertainty for the proposed measurement are acceptance corrections and particle identification.

The detector acceptance and polarized target magnetic field effect studies will be performed through simulations – the standard GEANT4 package.

As described in Sec. 3, lepton identification will be performed using the energy deposition in fine-granulated NPS. Protons will separate by TOF and $\frac{dE}{dx}$. All events used for the analysis of this proposed experiment will have both leptons detected in one of the NPS, and proton in one of Recoil hodoscopes.

6. BEAM TIME

This proposed experiment will require unpolarized 11 GeV beam and a transversely polarized proton (solid ammonia) target.

Experiment will use quasi-real photons (will not detect scattering electron), so will need detection and identification capability of all final products of TCS reaction (e^+ , e^- and p).

This would be accomplished by the high-resolution time-of-flight system and high energy resolution calorimetry.

To reach initial goal of proposal we require 30 days beam-time. The beam current will be limited by polarized target and need to keep in the on the level of ~ 100 nA.

-
- [1] K. Goeke and M.V. Polyakov and M. Vanderhaeghen, Hard exclusive reactions and the structure of hadrons, *Progress in Particle and Nuclear Physics*, 47 (2001) pp.401-515, arXiv:hep-ph/0106012.
- [2] M. Diehl, Generalized parton distributions, *Physics Reports* 388 (2003) pp.41-277
- [3] V. Belitsky and A.V. Radyushkin, Unraveling hadron structure with generalized parton distributions, *Physics Reports* 418 (2005) pp.1-387.
- [4] M. Guidal, H. Moutarde and M. Vanderhaeghen, *Rept. Prog. Phys.* 76 (2013) 066202.
- [5] M Guidal, H. Moutarde and M. Vanderhaeghen, Generalized Parton Distributions in the valence region from Deeply Virtual Compton Scattering, arXiv:hep-ph/1303.6600, 2013.
- [6] E. R. Berger, M. Diehl and B. Pire, Timelike Compton scattering: exclusive photoproduction of lepton pairs, *The European Physical Journal C*23 (2002) 675-689; arXiv:hep-ph/0110062.
- [7] A.T. Goritschig, B. Pire and J. Wagner, arXiv:1404.0713 [hep-ph]
- [8] M. Boer, M. Guidal, arXiv:1412.2036, Dec 2014; M. Boer, M. Guidal and M. Vanderhaeghen, arXiv:1501.00270, Jan 2015.
- [9] JLab experiment E12-12-001: Timelike Compton Scattering and J/ψ photoproduction on the proton in e^+e^- pair production with CLAS12 at 11 GeV, note = http://www.jlab.org/exp_prog/proposals/12/PR12-12-001.pdf.
- [10] X. Ji, *Phys. Rev. Lett.* 78, 610 (1997); *Phys. Rev. D*55, 7114 (1997).
- [11] Vanderhaeghen, M. and Guichon, Pierre A.M. and Guidal, M., Deeply virtual electroproduction of photons and mesons on the nucleon: Leading order amplitudes and power corrections, *Phys. Rev. D*60 (1999) 094017; arXiv:hep-ph/9905372.
- [12] M. Vanderhaeghen, P.A.M. Guichon and M. Guidal, *Phys. Rev. Lett.* 80 5064 (1998).
- [13] M. Guidal, M. V. Polyakov, A. V. Radyushkin and M. Vanderhaeghen, *Phys. Rev. D* 72 054013 (2005).
- [14] Polyakov, M. V. and Weiss, C., Skewed and double distributions in the pion and the nucleon, *Phys. Rev. D*60 (1999) 114017; arXiv:hep-ph/9902451.
- [15] Paremuzyan, R., Timelike Compton Scattering, Pn,D, Thesis, Yerevan, 2010.
- [16] Ibrahim H. Albayrak, Timelike Compton Scattering Analysis Note, The Catholic University of America, July, 2013.
- [17] Polyakov, M.V. and Shuvaev, A.G., On 'dual' parametrizations of generalized parton distributions, arXiv:hep-ph/0207153.
- [18] Guzey, V. and Teckentrup, T., The Dual parameterization of the proton generalized parton distribution functions H and E and description of the DVCS cross sections and asymmetries, *Phys. Rev. D*74 (2006) 054027; arXiv:hep-ph/0607099.
- [19] Polyakov, Maxim V. and Semenov-Tian-Shansky, Kirill M., Dual parametrization of GPDs versus double distribution Ansatz, *Eur. Phys. J.*, A40 (2009) 181-198; arXiv:0811.2901 [hep-ph].
- [20] Guzey, V. and Teckentrup, T., On the mistake in the implementation of the minimal model of the dual parameterization and resulting inability to describe the high-energy DVCS data, *Phys. Rev. D*79 (2009) 017501; arXiv:0810.3899 [hep-ph].
- [21] Radyushkin, A.V., Double distribution s and evolution equations, *Phys. Rev. D*59 (1999) 014030; arXiv:hep-ph/9805342.

- [22] M. Kubantsev et al., Performance of the Primex Electromagnetic Calorimeter, arXiv:physics/0609201, 22 Sep. 2006; A. Gasparyan, Performance of PWO crystal Detector for a High Resolution Hybrid Electromagnetic Calorimeter at Jefferson Lab., Proceed. X Int. Conf. Calorimetry in Particle Physics, Perugia, Italy, 29 March-2 April 2004, pp. 109-115.
- [23] Measurement of Semi-Inclusive π^0 Production as Validation of Factorization, JLab Experiment E12-13-007, R. Ent, T. Horn, H. Mkrtchyan and V. Tadevosyan spokespersons. Proposal approved in 2015 by JLab PAC40.
- [24] B. Seitz et al., Response of a scintillating fiber detector to proton and pion beams at GSI, INSTMETH-09.pdf
- [25] J. Mulholland, SANE's Measurement of the Proton's Virtual Photon Spin Asymmetry, A_1^p , at Large Bjorken x , Ph.D Thesis, University of Virginia, 2012.
- [26] Vilardi Ignazio, Detection of low momentum protons with the new HERMES recoil detector, Ph.D Thesis, Universita' degli Studi di Bari, 2006/2007; www-hermes.desi.de/notes/pub/08-LIB/vilardi.08-003.thesis.pdf.
- [27] J. Bisplinghoff et al. A scintillating fibre hodoscope for high rate applications. Nucl. Instr. and Meth. A, 490, 101111, 2002.
- [28] E.C. Aschenauer et al. Testrun results from prototype fiber detectors for high rate particle tracking. Nucl. Instr. and Meth. A, 424, 459469, 1999.
- [29] Alessandro Mapelli, "Scintillation Particle Detectors Based on Plastic Optical Fibers and Microfluidics", Ph.D Thesis, Ecole Polytechnique Federale de Lausanne, 2011; <http://jinst.sissa.it/jinst/theses/2011-JINST-TH-004.pdf>
- [30] The Charge Form Factor of the Neutron, JLab experiment E93-026, D. Day spokesperson.
- [31] Precision Measurement of the Nucleon Spin Structure Functions in the Region of the Nucleon Resonances, JLab experiment E01-006, O. Rondon Aramayo spokesperson.
- [32] Spin Asymmetries on the Nucleon Experiment: SANE, JLab experiment E07-003, S. Choi, Z.E. Meziani, O. Rondon-Aramayo spokespersons.
- [33] GeN Technical Note.
- [34] D. Crabb and D. Day, "The Virginia/Basel/SLAC polarized target: operation and performance during experiment E143 at SLAC". Nucl. Inst. Meth. A356, 9-19 (1995).
- [35] H. Zhu, "A Measurement of the Neutron Electric Form Factor in $\vec{D}(\vec{e}, e'n)p$ Quasi-elastic Scattering at $Q^2 = 0.5 (GeV/c)^2$ ". Ph.D. Dissertation, University of Virginia, Charlottesville (2000).
- [36] UVa target group web page: <http://twist.phys.virginia.edu/documents.html>.
- [37] Event generator for TCS.
- [38] Kessler, Paul, Photon fluxes and the EPA, note = <http://lss.fnal.gov/archive/other/lpc-94-35.pdf> ,
- [39] Beringer, J. and et al., The Review of Particle Physics, Phys. Rev. D86 (2012) 010001.
- [40] Guzey, V., Code for cross section calculations for Bethe-Heitler and Timelike Compton Scattering.